Lithos 248–251 (2016) 193–219

Contents lists available at ScienceDirect

Lithos

journal homepage: www.elsevier.com/locate/lithos

Invited review article

Global variations in abyssal peridotite compositions

Jessica M. Warren

Dept. of Geological Sciences, University of Delaware, Penny Hall, Newark, DE 19716, USA

ARTICLE INFO

Article history:
Received 28 March 2015
Accepted 24 December 2015
Available online 9 January 2016

Keywords:
Abyssal peridotite
Mid-ocean ridge
Partial melting
Melt–rock interaction
Mantle geochemistry
Pyroxenite

ABSTRACT

Abyssal peridotites are ultramafic rocks collected from mid-ocean ridges that are the residues of adiabatic decompression melting. Their compositions provide information on the degree of melting and melt–rock interaction involved in the formation of oceanic lithosphere, as well as providing constraints on pre-existing mantle heterogeneities. This review presents a compilation of abyssal peridotite geochemical data (modes, mineral major elements, and clinopyroxene trace elements) for >1200 samples from 53 localities on 6 major ridge systems. On the basis of composition and petrography, peridotites are classified into one of five lithological groups: (1) residual peridotite, (2) dunite, (3) gabbro-veined and/or plagioclase-bearing peridotite, (4) pyroxenite-veined peridotite, and (5) other types of melt-added peridotite. Almost a third of abyssal peridotites are veined, indicating that the oceanic lithospheric mantle is more fertile, on average, than estimates based on residual peridotites alone imply. All veins appear to have formed recently during melt transport beneath the ridge, though some pyroxenites may be derived from melting of recycled oceanic crust.

A limited number of samples are available at intermediate and fast spreading rates, with samples from the East Pacific Rise indicating high degrees of melting. At slow and ultra-slow spreading rates, residual abyssal peridotites define a large (0–15% modal clinopyroxene and spinel Cr# = 0.1–0.6) compositional range. These variations do not match the prediction for how degree of melting should vary as a function of spreading rate. Instead, the compositional ranges of residual peridotites are derived from a combination of melting, melt–rock interaction and pre-existing compositional variability, where melt–rock interaction is used here as a general term to refer to the wide range of processes that can occur during melt transport in the mantle. Globally, ~10% of abyssal peridotites are refractory (0% clinopyroxene, spinel Cr# > 0.5, bulk Al_2O_3 < 1 wt.%) and some ridge sections are dominated by harzburgites while lacking a significant basaltic crust. Abyssal ultramafic samples thus indicate that the mantle is multi-component, probably consisting of at least three components (lherzolite, harzburgite, and pyroxenite). Overall, the large compositional range among residual and melt-added peridotites implies that the oceanic lithospheric mantle is heterogeneous, which will lead to the generation of further heterogeneities upon subduction back into the mantle.

Contents

E-mail address: warrenj@udel.edu.

http://dx.doi.org/10.1016/j.lithos.2015.12.023

1. Introduction

Mantle upwelling beneath ocean ridges results in adiabatic decompression melting, producing oceanic crust (a layered mixture of basalt, diabase and gabbro) and lithospheric mantle (peridotite). The source mantle for this process is often referred to as depleted mantle (DM) and estimates of DM composition have been derived from global mid-ocean ridge basalt (MORB) and abyssal (i.e., seafloor) peridotite compositions (Salters and Stracke, 2004; Workman and Hart, 2005). However, studies of MORB and abyssal peridotite have also identified the occurrence of compositional heterogeneities in the mantle beneath mid-ocean ridges. For example, significant isotopic heterogeneity has been identified within individual dredges and individual ridge segments based on analysis of basalts (e.g., Dosso et al., 1999; Dupré and Allègre, 1983; Hamelin et al., 1985) and peridotites (e.g., Cipriani et al., 2004; Mallick et al., 2014; Mallick et al., 2015; Salters and Dick, 2002; Stracke et al., 2011; Warren et al., 2009). Isotopic variations in peridotites also indicate the existence of compositional anomalies that extend to small (sub-meter) length-scales (Harvey et al., 2006; Liu et al., 2008; Warren and Shirey, 2012).

At the same time that isotopic studies have demonstrated the existence of long-term compositional heterogeneity in the mantle, studies of trace elements in abyssal peridotites have shown that peridotites are not simply the residues of fractional melting. Instead, their composition is often altered by the passage of melt through the peridotite (e.g., Brunelli et al., 2006; Hellebrand et al., 2002b; Johnson and Dick, 1992). The most dramatic examples of this are the dunite channels that form during reactive melt flow in the shallow upper mantle (Kelemen et al., 1995). Other peridotites contain evidence for trapped melts in the form of websteritic and gabbroic veins (e.g., Constantin et al., 1995; Dantas et al., 2007; Tartarotti et al., 2002). Even if the majority of melts are extracted by focused melt flow (Kelemen et al., 1997), diffuse flow must also occur at various depths beneath ridges and some of the variability in peridotite compositions is related to fertilization by low volume (<1%) melt percolation (Seyler et al., 2001; Warren and Shimizu, 2010). Hence peridotites – and basalts – can be used to gain insight into both pre-existing source variability and the processes involved in melting and melt extraction to generate the oceanic crust.

This review presents a global compilation of abyssal peridotite geochemical data for >1200 samples, including both unveined and veined material. The compilation consists of mineral modal, mineral major element, and clinopyroxene trace element datasets. Of these, modal clinopyroxene, spinel Cr# (Cr/[Cr+Al]*100), and clinopyroxene rare earth element (REE) concentrations are the most useful parameters for exploring melting processes and source heterogeneity in peridotites. The comparable MORB major and trace element dataset consists of >10,000 samples (Gale et al., 2013; Lehnert et al., 2000) and has been used to provide constraints on mantle melting, source composition and temperature (e.g., Dalton et al., 2014; Gale et al., 2014). The peridotite dataset is an order of magnitude smaller as peridotites are less frequently sampled at ridges and harder to analyze due to alteration and low concentrations of many trace elements. However, peridotites provide complimentary information to MORBs, including constraints on the lower length-scale limit of mantle heterogeneity and evidence for ultra-refractory domains. Following the terminology of Byerly and Lassiter (2014), the terms fertile and infertile/refractory are used here to refer to major or trace element compositions that imply either limited or significant melt removal, while the terms enriched and depleted are used to refer to isotopic components.

The abyssal peridotite compilation presented here includes samples from six major mid-ocean ridges, from a total of 282 sites at 35 transform fault and 18 ridge segment localities (Fig. 1). While the term abyssal peridotite can refer to any seafloor sample of ultramafic rock, samples from subduction zones have been excluded as their compositions are influenced by additional processes. The degree to which abyssal peridotites are representative of the oceanic mantle as a whole remains uncertain, but as direct samples of the oceanic upper mantle they provide a reference point for understanding mantle processes. The other main types of tectonically exposed peridotites are ophiolites (oceanic lithosphere obducted onto continental crust) and orogenic massifs (ultramafic bodies exposed in mountain belts and lacking a crustal sequence), both of which are dissociated from the environment in which they first formed (see review by Bodinier and Godard, 2014). Additional mantle samples are brought to the surface as xenoliths in lavas, predominantly on continents, but occasionally on ocean islands (see reviews by Simon et al., 2008; Pearson et al., 2014).

Globally, abyssal peridotites show large compositional variations, which can be ascribed to a combination of processes: (1) variations in degree of melting, (2) pre-existing variability in mantle composition and (3) melt–rock interaction. In this paper, I assess the role of each process in generating the observed compositional range among global peridotites. Dis-entangling these processes is important for understanding how oceanic lithosphere forms, how the mantle has evolved over time, and how the mantle will continue to evolve when oceanic lithosphere is subducted.

2. Geographic coverage

Abyssal peridotites have been dredged at mid-ocean ridges since the 1960s (Bonatti, 1968; Engel and Fisher, 1969) and large geochemical datasets became available starting in the 1980s (Bonatti et al., 1992; Dick, 1989; Dick and Bullen, 1984; Dick et al., 1984). This review builds on these studies, presenting a compilation of 1268 peridotites from 282 sites (Table 1; see table footnote for the 65 references used to make the compilation). Samples from the Mid-Cayman Spreading Center have been excluded due to the complex tectonic history of this region (e.g., Hayman et al., 2011), which results in peridotites that are influenced by proximity to subducting crust.

Six major ridge systems (Fig. 1; see supplemental material for a KML file of sample locations) are represented in the dataset: the East Pacific Rise (EPR, full spreading rate = 128–157 mm/yr), the Central Indian Ridge (CIR, 26–50 mm/yr), the Mid-Atlantic Ridge (MAR, 21–36 mm/yr), the American-Antarctic Ridge (AAR, 17–19 mm/yr), the Southwest Indian Ridge (SWIR, 8–19 mm/yr), and the Gakkel Ridge

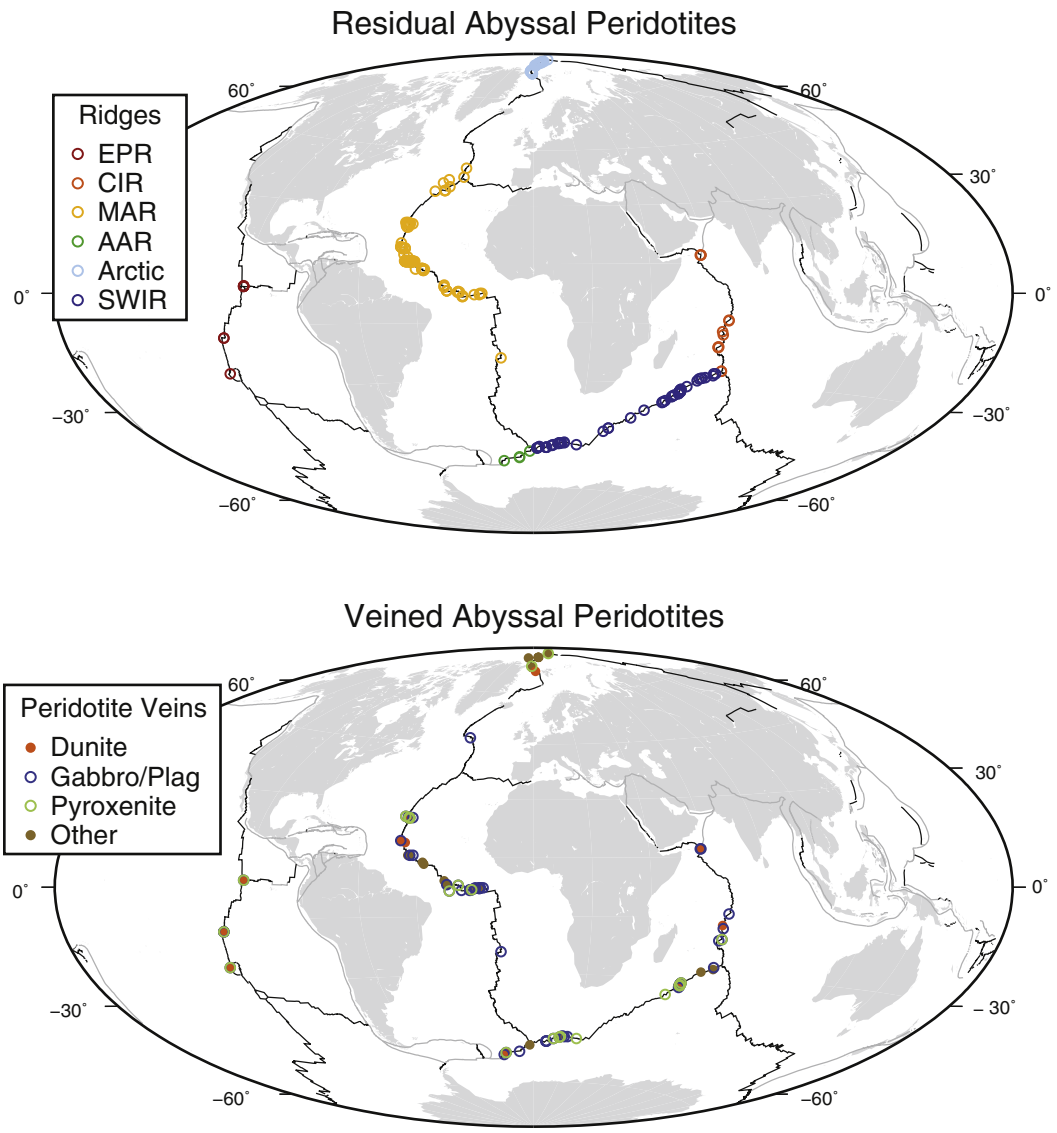

Fig. 1. Global distribution of residual (top) and veined (bottom) abyssal peridotites. Maps are based on sample locations for peridotites with published data and do not reflect the entire collection of abyssal peridotites that have been collected at ridges. Site locations and references are in Table 1. Residual peridotites have been filtered to remove any peridotites with veins, matrix plagioclase or modes that plot outside of the lherzolite/harzburgite fields. The ridge abbreviations are East Pacific Rise (EPR), Mid-Cayman Rise (MCR), Central Indian Ridge/Carlsberg Ridge (CIR), Mid-Atlantic Ridge (MAR), American-Antarctic Ridge (AAR), Gakkel Ridge/Lena Trough (Arctic) and Southwest Indian Ridge (SWIR). Veined peridotites are colored according to their dominant vein lithology.

and Lena Trough (Arctic, 11–14 mm/yr). Peridotites have not been collected at spreading rates between 50 and 128 mm/yr, which reflects the decrease in peridotite exposure as spreading rate increases and the difficulty of accessing some ridges. The Southeast Indian Ridge (~70 mm/yr) and Pacific–Antarctic Ridge (~85 mm/yr) are both located in remote regions of the southern oceans where sea conditions are usually rough.

Most abyssal peridotites have been collected by dredging, which represents a simple and efficient way to recover large volumes of rock. In addition, drill core samples are available from Hess Deep on the EPR and three MAR localities: Pico transform fault, Mid-Atlantic Ridge at Kane (MARK area), and Fifteen-Twenty transform fault. Finally, a small number of samples have been recovered by diving using submersibles and remotely operated vehicles, which provides geological context for samples, but fewer samples can be collected during a dive compared to a dredge.

The majority of peridotite samples have been collected from the walls of transform faults, where uplifted sections of oceanic lithosphere are exposed. More recently, on-axis peridotites have been collected from slow and ultra-slow spreading ridges following the identification of additional mechanisms for peridotite emplacement. At slow spreading ridges, oceanic core complexes expose blocks of lower crust and upper mantle through uplift on detachment faults (Cann et al., 1997; John and Cheadle, 2010; Smith et al., 2012). In addition, as spreading rate decreases below 40 mm/yr, on-axis conductive cooling becomes important in limiting melting and causing melt to freeze directly into the mantle, resulting in on-axis emplacement of peridotite (e.g., Bown and White, 1994; Cannat, 1996; Dick et al., 2003; Sauter et al., 2013). Five on-axis ridge segments have now been sampled extensively for peridotite: Lena Trough, the Gakkel Sparsely Magmatic Zone, the SWIR Oblique Segment, the easternmost SWIR at 62°–68°E, and Kane Megamullion on the MAR.

Despite increases in on-axis sampling, transform fault localities dominate, corresponding to 65% of localities and 57% of analyzed samples. The degree of melting beneath transform faults is expected to be lower than at ridges, due to the transform edge effect of juxtaposing older, colder lithosphere against new crust (e.g., Phipps Morgan and Forsyth, 1988). However, recent thermal models have shown that

Table 1
Summary of peridotite localities and lithologies in the global compilation.

Location	FSR (mm/yr)	Latitude	Longitude	Depth (mbsl)	# of Sites	Resid #[a]	Vein #[a]	Total #[a]	Lithology[b]	References[c]
East Pacific Rise (EPR)										
Terevaka TF	157	24.24°S	115.69°W	4200	1	4	27	31	Harz; dunite, Pl-dunite; veins of gabbro, ferro-gabbro, Cpxite	1
Garrett TF	150	13.48°S	111.55°W	3800–4892	5	4	28	32	Harz; Pl-harz, Amph-harz, dunite, Pl-dunite, wehrlite; gabbro veins	1–3
Hess Deep	134	2.28°N	101.45°W	3693–3821	6	20	12	32	Harz; Pl-harz, dunite, Pl-dunite, wehrlite	5, 6
Central Indian Ridge (CIR)										
Green Rock Hill	50	25.4°S	69.76°E		2	3	0	3	Harzburgite	7
Marie Celeste TF	41	17.05°S–17.65°S	65.61°E–66.87°E	3500–5185	4	10	5	15	Harz; Pl-lherz, Pl-harz; Ol-webst veins	7–10
Ridge at 12°S	36	12.42°S	65.93°E	3730	1	3	1	4	Harz; dunite	7
Argo TF	38	13.57°S	66.46°E	3560–4225	2	3	2	5	Lherz, harz; Pl-harz	7, 10
Vema II TF	37	8.69°S–8.92°S	67.63°E	3030	2	5	1	6	Harz; magmatic vein	7–9
Owen TF	26	12.58°N–12.62°N	58.13°E–58.29°E	1450–2530	3	11	4	15	Lherz, harz; Pl-lherz, dunite	11
Mid-Atlantic Ridge (MAR)										
Gibbs TF	23	52.03°N	31.52°W		1	0	1	1	Lherz with gabbro vein	12
Ridge at 43°N	24	43.21°N	28.93°W	2250	1	8	0	8	Harzburgite	13
Kurchatov TF	24	40°N	29°W		1	1	0	1	Harzburgite	14
Pico TF	21	37.77°N–38.94°N	34.69°W–36.66°W	3672–3754	2	14	0	14	Harzburgite	15
Famous TF	21	36.59°N	33.55°W	2437	1	1	0	1	Harzburgite	14
Oceanographer TF	22	34.72°N–35.13°N	35.03°W–38.84°W	3443	4	5	0	5	Harzburgite	15
Kane TF	25	23.52°N–23.8°N	43.91°W–46.57°W	2900–4840	13	25	7	32	Lherz, harz; Pl-harz, dunite; Ol-webst vein	16–19
Kane MARK	25	22.22°N–23.34°N	45.02°W–46.08°W	2250–4480	7	107	19	126	Lherz, harz; dunite, Ol-webst, Amph-harz; gabbro veins	18, 20–26
Kane Megamullion	25	23.28°N–23.61°N	45.28°W–45.42°W	2407–3462	15	41	66	107	Lherz, harz; Pl-lherz, Pl-harz, dunite, Pl-dunite, Ol-webst, Opxite; veins of gabbro, Ol-gabbro, Ox-gabbro, Gb-norite, troctolite	18, 27
Ridge at 17°N	26	16.87°N	46.5°W	4000	1	1	0	1	Harzburgite	28
Fifteen-Twenty TF	27	15.04°N–15.65°N	44.85°W–46.68°W	2700–4100	8	52	19	71	Harz; dunite; other metasom; gabbro veins	28–31
Marathon TF	25	12.95°N	44.95°W	2200	1	2	0	2	Peridotite	31
Mercurius TF	26	12.12°N	43.52°W	3000	1	3	0	3	Peridotite	31
Vema TF	28	10.65°N–10.94°N	41.06°W–44.59°W	2880–5070	52	167	4	171	Lherz, harz; Pl-perid, Amph-perid; magmatic vein	12, 32–36
Doldrums TF	29	7.75°N–8.3°N	37.45°W–40.58°W	2020–4500	13	18	2	20	Perid; Other metasom	31
Ridge at 2–4°N	31	2.1°N–2.92°N	30.31°W–30.42°W	2070–2690	3	6	1	7	Perid; Other metasom	31
St Paul TF	32	0.37°N–0.99°N	25.04°W–29.4°W	2300–3950	4	10	0	10	Peridotite	31
SPTF: St Paul's Rocks	32	0.82°N	29.49°W	1319–1587	1	2	4	6	Lherz, harz; Pl-harz	37
SPTF: ITR-A	32	0.73°N	25.52°W	4347–4728	1	8	3	11		37
Romanche TF	32–33	1.21°S–0.03°N	17.03°W–28.54°W	1380–7200	20	13	33	46	Lherz, harz; Pl-lherz, Pl-harz, Pl-Ol-webst; Other metasom	8, 9, 12, 36, 38, 39
22°S TF	36	21.93°S	11.8°W	1860	1	4	1	5	Harz; Pl-lherz	8, 9, 16
American-Antarctic Ridge (AAR)										
Conrad TF	19	55.5°S	2.1°W	1080	1	6	1	7	Harz; Amph-harz	40
Bullard TF	17–18	57.78°S–58.43°S	7.67°W–15.66°W	2920–3684	3	22	7	29	Lherz, harz; Pl-lherz, Pl-harz, Pl-dunite, Pl-wehrlite	41, 42
Vulcan TF	17	59.09°S	16.81°W	3379	1	15	7	22	Lherz, harz; Pl-lherz, Pl-harz; gabbro vein	41, 42
Southwest Indian Ridge (SWIR)										
Bouvet TF	14	53.81°S–54.49°S	1.57°E–3°E	400–4170	5	18	0	18	Harzburgite	9, 40–43
Islas Orcadas TF	14	54.07°S	6.29°E	2340–3650	4	20	8	28	Lherz, harz; Pl-lherz, Pl-harz	9, 41–44
Shaka TF	14	53.4°S	9.15°E	4063–4207	2	6	0	6	Lherzolite	42–45
Oblique Segment	8–14	52.1°S–53.14°S	9.98°E–16.64°E	3128–4361	11	35	39	74	Lherz, harz; Pl-lherz, Pl-harz, webst, Ol-webst, Pl-Ol-webst; veins of gabbro, webst, Ol-webst, Pl-Ol-webst, Opxite	16, 42, 45–48
Orthogonal Segment	14	53.05°S	21.38°E	3992	1	3	2	5	Harz; Ol-webst, Opxite	45
Andrew Bain TF	15	47.7°S	32.15°E	4000	1	1	0	1	Lherzolite	42
Prince Edward TF	15	46.52°S	33.81°E	2700–5100	2	5	0	5	Harzburgite	42, 44
Discovery II TF	15	42.69°S	41.89°E	4400	1	1	0	1	Lherzolite	42
Indomed TF	15	39.79°S	45.99°E	1950	1	1	0	1	Lherzolite	42
Gallieni TF	15	36.65°S–36.85°S	52.11°E–52.41°E	575–4750	3	16	0	16	Lherz, harz	44, 49
Ridge at 53–56°E	15	34.03°S–36.14°S	52.99°E–55.83°E	3800–4200	5	28	1	29	Lherz, harz	50, 51
Atlantis II TF (AIITF)	15	32.11°S–33.63°S	56.86°E–57.35°E	1356–5133	13	21	24	45	Lherz, harz; Pl-lherz, Pl-harz, dunite, Ol-webst, Pl-Ol-webst; gabbro vein	10, 44, 47, 52, 53

Table 1 (*continued*)

Location	FSR (mm/yr)	Latitude	Longitude	Depth (mbsl)	# of Sites	Resid #[a]	Vein #[a]	Total #[a]	Lithology[b]	References[c]
Southwest Indian Ridge (SWIR)										
AIITF: Ridge-Transform Intersection (RTI)	15	31.93°S	57.15°E	3500–4988	2	3	6	9	Lherz; other metasom; veins of gabbro, clinopyroxenite	45, 46
AIITF: Atlantis Bank	15	32.56°S–32.91°S	57.13°E–57.21°E	2564–4974	10	38	9	47	Lherz, harz; Pl-lherz, webst, Ol-webst, dunite; other metasom; gabbro veins	45, 47, 52–57
Ridge at 59°E	15	31.04°S	59.12°E	5000	1	3	0	3	Harzburgite	50, 51
Ridge at 62–68°E	14	26.49°S–28.88°S	61.94°E–67.98°E	2225–5050	8	29	3	32	Lherz, harz; Pl-lherz; other metasom	9, 10, 14, 50, 51, 58
Gakkel Ridge, Lena Trough, & Molloy Ridge (Arctic)										
Gakkel Eastern Volcanic Zone (EVZ)	11–12	86.26°N–86.8°N	34.75°E–67.72°E	3872–4876	3	9	3	12	Lherz, harz; Ol-webst; other metasom	59–61
Gakkel Sparsely Magmatic Zone (SMZ)	12–13	84.49°N–86.01°N	14.98°W–26.8°E	2809–4978	14	27	4	31	Lherz, harz; other metasom	59–62
Lena Trough	14	80.91°N–82.32°N	2.46°W–5.57°W	2912–3983	12	48	7	55	Lherz, harz; webst, Ol-webst, Pl-Ol-webst, Cpxite, Pl-opxite; other metasom; webst vein	63–65
Molloy Ridge	14	79.38°N	2.65°E	2000	1	0	1	1	Dunite	44
Totals					282	906	362	1268		

[a] Total = total number of samples; Resid = residual peridotites; Vein = veined peridotites.

[b] Abbreviations: Lherz = lherzolite; Harz = harzburgite; Pl = plagioclase; Ol = olivine; Amph = amphibole; Webst = websterite; Opxite = orthopyroxenite, Cpxite = clinopyroxenite; Other metasom refers to melt-added peridotites that do not contain veins in hand sample (see description in text).

[c] References: 1 = Constantin et al. (1995), 2 = Constantin (1999), 3 = Cannat et al. (1990), 4 = Niu and Hékinian (1997a), 5 = Dick and Natland (1996), 6 = Arai and Matsukage (1996), 7 = Hellebrand et al. (2002a), 8 = Bryndzia et al. (1989), 9 = Bryndzia and Wood (1990), 10 = Dick et al. (1984), 11 = Hamlyn and Bonatti (1980), 12 = Seyler and Bonatti (1997), 13 = Shibata and Thompson (1986), 14 = Dick and Bullen (1984), 15 = Michael and Bonatti (1985b), 16 = Mallick et al. (2014), 17 = Michael and Bonatti (1985a), 18 = Ghose et al. (1996), 19 = Luguet et al. (2003), 20 = Juteau et al. (1990), 21 = Komor et al. (1990), 22 = Niida (1997), 23 = Ross and Elthon (1997), 24 = Stephens (1997), 25 = Fujii (1990), 26 = Kempton and Stephens (1997), 27 = Dick et al. (2010), 28 = Cannat et al. (1992), 29 = Takahashi et al. (2007), 30 = Seyler et al. (2007), 31 = Bonatti et al. (1992), 32 = Brunelli et al. (2006), 33 = Cipriani et al. (2009b), 34 = Cipriani et al. (2009a), 35 = Cannat and Seyler (1995), 36 = Prinz et al. (1976), 37 = Brunelli and Seyler (2010), 38 = Tartarotti et al. (2002), 39 = Bonatti et al. (1993), 40 = Brunelli et al. (2003), 41 = Dick (1989), 42 = Johnson et al. (1990), 43 = Snow (1993), 44 = Jaroslow et al. (1996), 45 = Warren (2007), 46 = Warren et al. (2009), 47 = Salters and Dick (2002), 48 = Dantas et al. (2007), 49 = Zhou and Dick (2013), 50 = Seyler et al. (2003), 51 = Seyler et al. (2011), 52 = Coogan et al. (2004), 53 = Johnson and Dick (1992), 54 = Warren and Shimizu (2010), 55 = Kumagai et al. (2003), 56 = Morishita et al. (2007), 57 = Achenbach (2008), 58 = Seyler et al. (2004), 59 = Hellebrand et al. (2005), 60 = Liu et al. (2008), 61 = (D'Errico et al., 2016), 62 = Hellebrand et al. (2002b), 63 = Hellebrand and Snow (2003), 64 = Lassiter et al. (2014), and 65 = Laukert et al. (2014).

the transform edge effect on thermal structure is relatively small when fault rheology is incorporated into the model (Behn et al., 2007; Roland et al., 2010). Thus, compositional differences among peridotites from transform faults versus ridge axes are not expected to be significant and data from the two types of localities have been combined.

The distribution and number of samples analyzed at any locality are variable, reflecting tectonic control on peridotite exposure, the extent of sampling carried out in an area, and the degree of post-cruise analytical work. The number of sites and number of samples per site also reflects the variability in peridotite outcrops — some areas have yielded multiple dredges containing many samples, whereas other areas have yielded either very few samples or highly altered samples that have not been analyzed further. Some dredges have undergone so much hydrothermal alteration that even spinel is not analyzable, whereas all mineral phases are analyzable in other dredges. Fresh peridotites have been recovered from the CIR (dredge CIRCE-97), SWIR (dredges AII107-60 and AII107-61), and Gakkel Ridge (dredges HLY102-40, HLY102-70, PS59-235, and PS66-238), though even these samples have minor serpentinization and do not look pristine in hand sample.

The best sampled and studied ridge system for peridotite is the MAR, with 648 peridotites from 150 sites across 21 localities, followed by the SWIR, with 320 peridotites from 69 sites across 16 localities (Table 1). The CIR, AAR and Arctic have limited numbers of samples, which reflects a lack of cruises to these regions. The EPR dataset is also sparse – despite many cruises to this ridge – and consists of 95 peridotites from 14 sites at only 3 localities. Very few peridotites outcrop at fast spreading rates as the basaltic crust is usually continuous. Hess Deep is one of the few major peridotite localities for the EPR, but is a tectonically unusual region adjacent to the Galapagos microplate (e.g., Floyd et al., 2002; Lonsdale, 1988). In contrast, many MAR and SWIR peridotites come from typical localities where peridotite is emplaced on-axis through fault uplift.

Overall, localities with the most comprehensive peridotite datasets are the Atlantis II transform fault on the SWIR, and the Vema, Kane and Fifteen-Twenty transform faults on the MAR. The Atlantis II transform fault has been sampled during 7 cruises, including detailed sampling of the transform fault (45 peridotites), ridge–transform intersection (9 peridotites) and the fossil oceanic core complex Atlantis Bank (47 peridotites). On the MAR, multiple cruises have resulted in 171 peridotites being analyzed from the Vema transform fault and 71 peridotites from the Fifteen-Twenty transform fault. Around the Kane transform fault, 32 peridotites have been analyzed from the fault itself, 126 from the MARK ridge section, and 107 from Kane Megamullion, a fossil core complex now located off-axis by ~3 Ma.

Veined peridotites have been found at 73% of locations with residual peridotites (Table 1), excluding localities where data is only available for one sample. The abundance of vein lithologies represents a minimum estimate, as some studies have either avoided analyzing veined peridotites or focused on specific vein types. Estimating abundances directly from dredge descriptions is currently limited by the lack of digital records for older cruises. Calculating the relative percentages of gabbros, pyroxenites, and dunites is complicated by the fact that many of these occur as composite samples (e.g., gabbro veins often occur in dunites). Statistics for Kane Megamullion probably represent the best estimate available for the relative proportions of different lithological types at a locality, as the full spectrum of veined and unveined peridotites were analyzed by Dick et al. (2008, 2010).

3. Peridotite categories

Data for 1268 peridotites are presented as supplementary tables, with data for 906 residual peridotites in Table S1 and for 362 veined peridotites in Table S2. The classification of abyssal peridotites as residual or veined is based on their petrographic descriptions and modal analyses. Among veined peridotites, samples are further subdivided based on vein composition and other evidence for melt addition (dunite, gabbro, pyroxenite, other metasomatism).

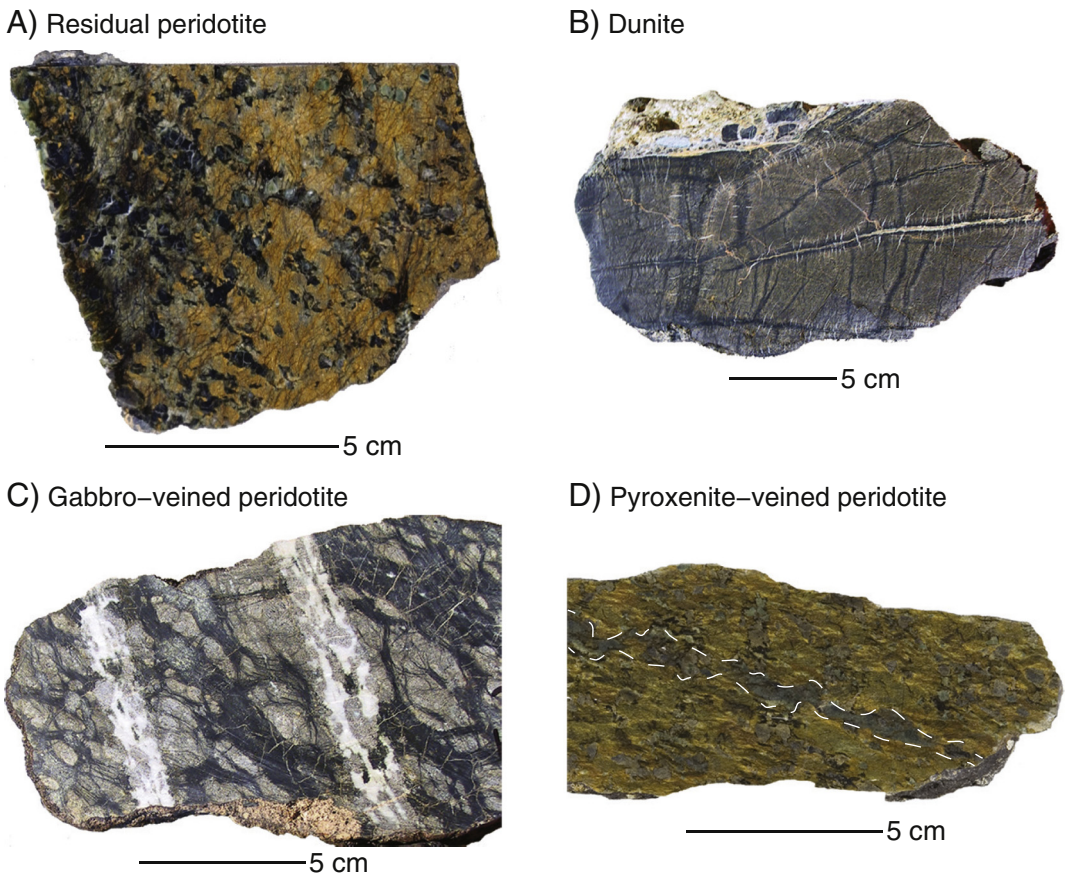

Fig. 2. Photos of hand samples of abyssal peridotites, all from the Oblique Segment of the SWIR. (A) Van7-85-30: harzburgite, with darker coloration on left side due to increased alteration. (B) Van7-78-13: dunite, consisting of olivine replaced by serpentine. Cross-cutting veins are also serpentine and white rind on top left is carbonate cement. (C) Van7-78-31: plagioclase peridotite cross-cut by two gabbro veins and later serpentine (dark gray) alteration. Plagioclase (white) is completely altered in both the peridotite matrix and the veins. (D) Van7-96-21: harzburgite with pyroxenite vein outlined by dashed white lines.

3.1. Residual peridotites [71% of samples]

Peridotites are classified as residual (Table S1) if they contain no cross-cutting veins or interstitial plagioclase, both of which are evidence of melt addition. For datasets that do not include lithological descriptions, samples are assumed to fall into this category unless trace elements or spinel Cr# indicate otherwise. This assumption probably under-estimates the number of plagioclase peridotites, as trace (<1%) plagioclase is difficult to identify without careful petrographic analysis or point counting.

Residual peridotites (Fig. 2A), as with all abyssal peridotites, have undergone variable degrees of alteration. Spinel is the most resilient phase to alteration and hence has the most compositional data in the compilation. Olivine is usually the most altered mineral, as it reacts faster than pyroxene at temperatures below ~250 °C to form serpentine, magnetite, and brucite (Bach et al., 2004; Klein et al., 2009). Pyroxene is less susceptible to serpentinization at these temperatures, but above ~350 °C reacts with seawater to form tremolite and talc, while olivine is stable (Bach et al., 2004).

In the abyssal peridotite literature, residual peridotites have received the most attention as they are considered to be representative of upper mantle composition following melt extraction. Subsets of residual peridotites have been used to estimate the composition of the model DM source (e.g., Salters and Stracke, 2004; Workman and Hart, 2005). However, recent studies have suggested that even residual peridotites have undergone some degree of melt–rock interaction, as discussed below.

3.2. Dunites [6% of samples]

Samples with >90% olivine are classified as dunites (Fig. 2B). Many dunites contain either gabbro or pyroxenite veins, while some dunites themselves occur as veins within peridotite. Dunites are interpreted as porous flow channels by which most melt is transported out of the mantle (Kelemen et al., 1995, 1997). The occurrence of gabbro or pyroxenite veins that are separated from the adjacent peridotite by dunite agrees with this model. Many dunites are highly altered, with olivine completely serpentinized, indicating the greater susceptibility of olivine aggregates to hydrothermal alteration compared to aggregates of olivine plus pyroxene. Spinels are frequently the only analyzable mineral in dunites and their major element composition represents the largest geochemical dataset for this lithology (Table S2). Only 3 of 81 dunites have clinopyroxene trace element data, due to the scarcity of clinopyroxene in dunites and overall high levels of alteration.

3.3. Gabbro-veined and/or plagioclase-bearing peridotites [15% of samples]

This group (abbreviated name: gabbro/plag peridotites), consists of peridotites with gabbro veins and/or interstitial plagioclase (Fig. 2C). Plagioclase can be easy to identify in hand sample as it is highly susceptible to alteration, which turns it from translucent white to opaque white (Fig. 2C). However, this limits the collection of compositional data and only 44 out of 194 gabbro/plag peridotite samples have plagioclase major element data (last set of data columns in Table S2).

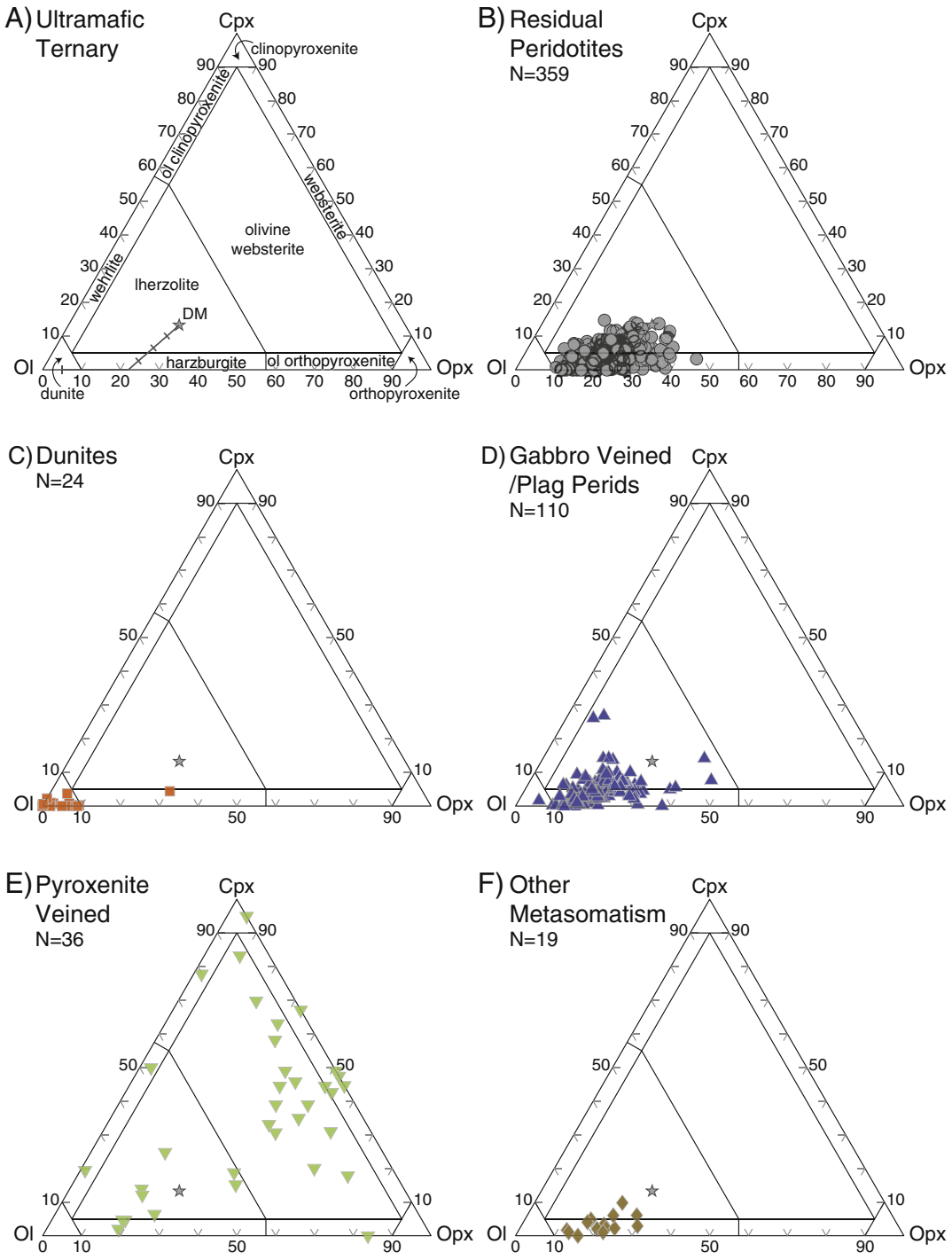

Fig. 3. Peridotite modes plotted on the ultramafic ternary by lithologic type. Residual peridotites plot entirely within the lherzolite and harzburgite fields, as mineral modes were used as a criteria for identifying residual peridotites. Plagioclase-bearing samples have been plotted with mineral modes renormalized on a plagioclase-free basis as they contain <3% plagioclase on average (Table S2). The star indicates the model depleted mantle (DM) source composition from Workman and Hart (2005), which has an estimated 13% clinopyroxene. The gray line in (A) shows the degree of melting for the 1 GPa melting reaction $0.56Opx + 0.72Cpx + 0.04Spin = -0.34Oliv + 1Melt$ from Wasylenki et al. (2003), with tick marks indicating increments of 5% melting.

Samples are plotted on the ultramafic ternary (Fig. 3D) on a plagioclase-free basis by re-calculating the relative proportions of olivine, orthopyroxene and clinopyroxene assuming that their mineral modes sum to 100%. This simplification allows comparison to the other peridotite categories (Fig. 3), but does not represent the lithological variations within this group due to variations in plagioclase mode (0.01% to 30%) relative to other phases that may have increased in proportion due to melt crystallization, such as clinopyroxene. The veins themselves span a range of compositions, including gabbro, olivine gabbro, oxide gabbro, norite, and troctolite.

Any peridotite with plagioclase disseminated in the matrix of the peridotite has been included in this category – even if it does not have a vein – as plagioclase in abyssal peridotites is interpreted as indicating melt infiltration (e.g., Chalot-Prat et al., 2013; Dick, 1989; Dijkstra et al., 2001; Müntener et al., 2010; Piccardo et al., 2007; Seyler and Bonatti, 1997; Warren and Shimizu, 2010). Many experiments indicate that

spinel should break down to plagioclase at pressures of ~1–1.5 GPa or ~30–45 km (Gasparik, 1987; Green and Ringwood, 1968; Kushiro and Yoder, 1966; Walter and Presnall, 1994), yet most abyssal peridotites contain spinel instead of plagioclase. However, most of these experiments were done on simplified systems that, in particular, do not contain Cr-spinel (chromite). Experiments on more complex chemical systems, particularly those including Cr, Ti, Na, and Fe, demonstrate that spinel becomes stable to lower pressures, with breakdown to plagioclase not occurring until pressures <0.8 GPa (e.g., Asimow et al., 1995; Borghini et al., 2010; Falloon et al., 2008; Green and Hibberson, 1970). At these shallow depths, abyssal peridotite temperatures may be too low for breakdown to occur. Hence, plagioclase in abyssal peridotites, even peridotites with <1% plagioclase, is assumed to represent melt infiltration.

3.4. Pyroxenite-veined peridotites [5% of samples]

This group consists of clinopyroxenite, orthopyroxenite, wehrlite, websterite and olivine websterite, which occur either as veins enclosed in peridotite or dunite, or on their own (Fig. 2D). On the ultramafic ternary (Fig. 3E), these samples correspond to the pyroxene-rich, olivine-poor lithologies that do not plot in the lherzolite, harzburgite, or dunite fields. However, as the host peridotite is included with the vein in this category, a few lherzolites and harzburgites show up on the ternary in Fig. 3E.

Two main origins have been assigned to pyroxenites: (1) recycling of oceanic crust or (2) recent melt crystallization. Pyroxenites that correspond to pieces of recycled oceanic crust are often referred to as primary pyroxenites and should have silica-enriched compositions corresponding to eclogite or garnet-bearing websterite (e.g., Pertermann and Hirschmann, 2003). In contrast, secondary pyroxenites form by crystallization of partial melts of peridotite or pyroxenite. The major element composition of pyroxenite-derived melts and peridotite-derived melts can be similar, making the source lithology for secondary pyroxenite veins difficult to determine (Lambart et al., 2009). In addition, pyroxenite-derived melts can undergo significant reaction with surrounding peridotites, unless they are isolated in dunite channels (Lambart et al., 2013). Thus, secondary pyroxenites can have a large range of compositions, from silica-poor (e.g., wehrlite, olivine websterite) to silica-enriched (e.g., clinopyroxenite, garnet-bearing websterite). Textural relationships can sometimes provide information on pyroxenite origin, particularly if the pyroxenite cross-cuts the host peridotite foliation, which would suggest recent formation.

Pyroxenites in this compilation cover a large compositional range, but the majority are olivine websterites (i.e., silica-poor). On the basis of petrographic and compositional evidence for recent crystallization, all ridge pyroxenites have so far been classified as secondary (Brunelli and Seyler, 2010; Constantin, 1999; Constantin et al., 1995; Dantas et al., 2007; Laukert et al., 2014; Tartarotti et al., 2002; Warren et al., 2009).

3.5. Other metasomatized peridotites [2% of samples]

A small subset (30 samples) of abyssal peridotites have no veins, but show other evidence for recent addition of melt based on detailed petrographic and/or compositional analyses. Peridotites in this subset have one or more of the following characteristics: (i) mineral inclusions (Seyler et al., 2004); (ii) trace element enrichments, particularly if normalized values of light rare earth elements ($LREE_N$) are greater than heavy rare earth elements ($HREE_N$) (Warren and Shimizu, 2010; D'Errico et al., 2016); (iii) high (>1 wt.%) TiO_2 concentrations in spinel (Dick and Bullen, 1984); or (iv) amphibole (Cannat and Seyler, 1995). Peridotites in this category are referred to by the term "other metasomatized", where the term metasomatism is used here as a shorthand to indicate "melt-added peridotite that does not contain visible veins in hand sample". Some of these samples may have been located adjacent to veins or they may reflect more diffuse melt flow through peridotite.

Due to the detailed petrographic and compositional analyses often necessary to identify peridotites in this group, their abundance is probably underestimated. However, these samples can provide information on processes that occur during melt extraction. Modeling of peridotites with $LREE_N > HREE_N$ has shown that these trace element patterns can only be produced by crystallization of small volumes of low-degree melts (Brunelli et al., 2014; D'Errico et al., 2016). Warren and Shimizu (2010) found orders of magnitude variation in clinopyroxene trace element concentrations at the sub-sample length-scale in three abyssal peridotites. As variations at this length-scale will diffusively equilibrate over timescales of <1 My at upper mantle temperatures, these peridotites must have undergone recent, shallow-level interaction with melt. Seyler et al. (2004) reached a similar conclusion for orthopyroxene-hosted mineral inclusions in residual peridotites.

4. Datasets

Tables S1 (residual peridotites) and S2 (veined peridotites) present data for mineral modes, major element compositions of the main mineral phases (olivine, orthopyroxene, clinopyroxene, and spinel, plus plagioclase in Table S2), and trace element compositions of clinopyroxene. The methodology is standard for each of these techniques and only a brief summary is given below. The full spreading rate at each sample location was calculated using the Lamont–Doherty Plate Velocity Calculator using NUVEL-1 (Argus and Gordon, 1991). For the SWIR Oblique Segment, the full spreading rate was converted to effective spreading rate, which takes into account obliquity of the ridge axis to the plate spreading direction, following the method of Abelson and Agnon (1997).

Modal clinopyroxene, spinel Cr#, and clinopyroxene trace elements are highlighted in Figs. 3–9 as these represent the most useful parameters for interpreting peridotite compositions. With increasing degree of melting, modal clinopyroxene decreases as melting of ultramafic compositions consumes clinopyroxene (Dick et al., 1984; Kinzler and Grove, 1992). Spinel Cr# increases while spinel Mg# (Mg / [Mg + Fe]) decreases during melting, as Al and Mg preferentially go into the melt relative to Cr and Fe (Dick and Bullen, 1984). Olivine Mg# also decreases during melting (Arai, 1987), but spinel is more useful as it is more commonly preserved in seafloor samples. All the trace elements presented in Tables S1 and S2 are incompatible in clinopyroxene during melting. The degree of melting is best reflected by the heavy rare earth elements (HREE: Tb through Yb), which are less susceptible to melt–rock interaction compared to more incompatible elements, such as the light rare earth elements (LREE: La through Gd).

Bulk rock Al_2O_3 is another parameter used to determine the degree of fertility in peridotites, but is not included in this compilation. Relatively few studies have measured bulk rock compositions in abyssal peridotites due to concerns about the influence of alteration on composition, though some elements (such as Al and REEs) are much less affected by seawater alteration than other elements (Si, Ca, Sr) (e.g., Niu, 1997, 2004; Seyfried et al., 2007; Malvoisin, 2015). Hence, bulk rock data is only available for <400 abyssal peridotites, of which only ~30% of samples overlap with the mineral-specific dataset presented here. In addition, the bulk rock dataset does not provide sufficient global coverage, as ~30% are from the Fifteen-Twenty transform fault (Paulick et al., 2006; Godard et al., 2008) and ~40% are from the SWIR (Niu, 2004).

Another dataset not included in this compilation is the long-lived radiogenic isotopes, which provide direct constraints on the long-term depletion or enrichment of peridotites. Only ~100 abyssal peridotites have been measured for isotopes, largely due to low concentration levels and the difficulty of analyzing altered samples. Recent studies have reviewed the global isotope datasets for Sr and Nd (Warren et al., 2009), Hf (Byerly and Lassiter, 2014), Pb (Warren and Shirey,

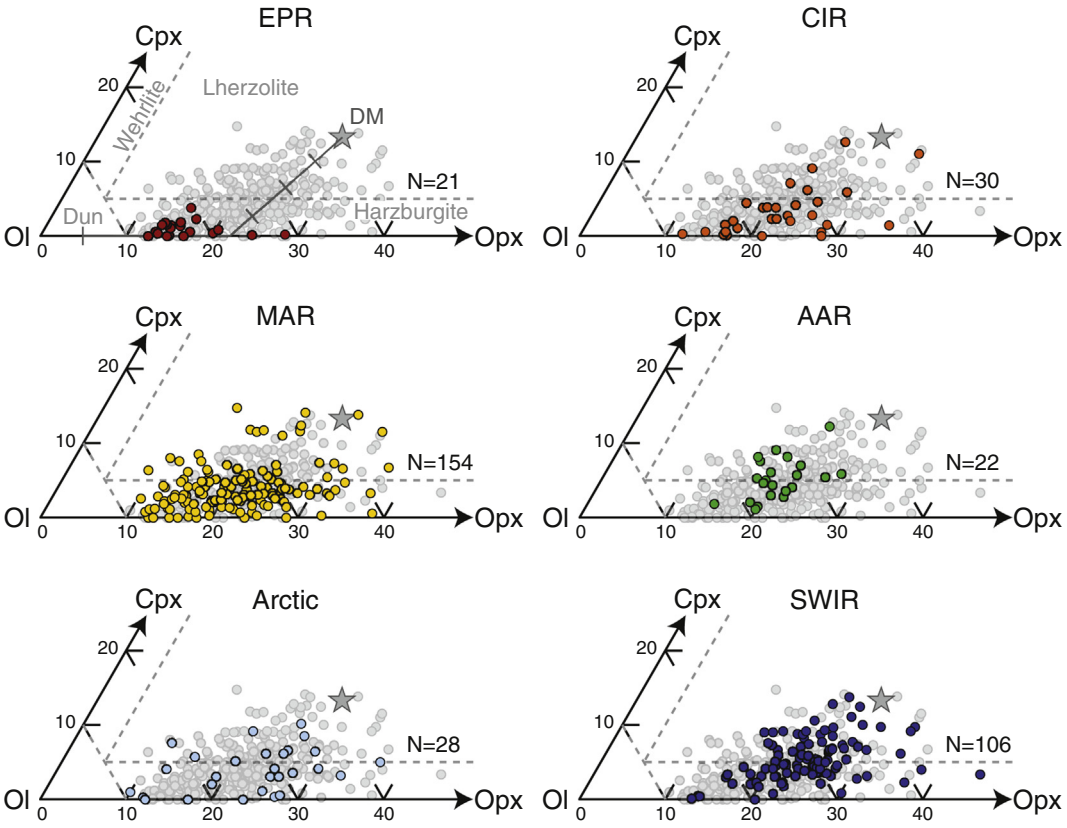

Fig. 4. Residual peridotite modal compositions plotted on the ultramafic ternary (full ternary is shown in Fig. 3). The gray symbols in the background are the global dataset for residual peridotites. Gray dashed lines delimit fields for the different ultramafic lithologies. The composition of DM (gray star) is from Workman and Hart (2005). The gray line in the EPR figure indicates the evolution of mineral modes during melting for the 1 GPa reaction $0.56Opx + 0.72Cpx + 0.04Spin = -0.34Oliv + 1Melt$ from Wasylenki et al. (2003), with tick marks indicating increments of 5% melting.

2012), and Os (Alard et al., 2005; Lassiter et al., 2014; Harvey et al., 2015), as well as compared abyssal peridotites to Alpine–Apennine ophiolites (Rampone and Hofmann, 2012). Given the small number of samples with isotope data that overlap with the modal/major/trace dataset presented here, future comparisons of the relationship between peridotite fertility/infertility and isotopic enrichment/depletion would be aided by expanding the isotopic dataset.

4.1. Modal data

Mineral modes are plotted on the ultramafic ternary (olivine–orthopyroxene–clinopyroxene) by lithology in Fig. 3 and by ridge for residual peridotites in Fig. 4. Identification of lithology is based on observation of hand samples (e.g., identification of veins and estimation of mineral proportions), followed by point counting of mineral modes. Modal data are collected on thin sections, typically using large format (50 × 76 mm) sections and counting >2000 points on a 1 mm grid. The melting trajectory for DM mantle is shown in Figs. 3–4, calculated using the lever-rule to predict changes in phase proportions during melting for the reaction $0.56Opx + 0.72Cpx + 0.04Spin = -0.34Oliv + 1Melt$ (Wasylenki et al., 2003). This trajectory defines a much narrower compositional range than represented by the peridotite dataset. However, the calculation does not take into account changes in the melting reaction as a function of depth or the influence of variable source composition and melt–rock interaction.

Globally, harzburgites (i.e., <5% clinopyroxene) represent 66% of residual peridotites and are overall the most abundant lithology among all ultramafic sample types (Fig. 3). Among veined peridotites, gabbro/plagioclase peridotites are the most abundant, representing 54% of veined samples.

The largest modal datasets are from the MAR and SWIR for both veined and unveined peridotites (Fig. 4). SWIR residual peridotites are evenly split between lherzolites (51%) and harzburgites (49%), whereas MAR peridotites are predominantly harzburgites (75%). However, this may reflect oversampling on the MAR of specific localities (Kane and Fifteen-Twenty fracture zones), whereas the SWIR dataset is more evenly spread along the ridge (Fig. 1). Approximately 10 MAR samples plot off the global trend towards higher Cpx contents (Fig. 4), but this does not appear to be a site-specific or analytical issue as these data are from 5 different locations and collected by 7 different authors.

The EPR is notable for having only harzburgites, though geographic coverage is limited to three localities (Fig. 1). However, other ridges with few sample localities, such as the CIR (five localities) and AAR (three localities) have both lherzolites and harzburgites. This suggests that the EPR, which is the fastest spreading ridge, is systematically more refractory than other ridges, particularly as EPR peridotites also have refractory major and trace element compositions.

Garnet and amphibole are notably lacking in abyssal peridotites. Garnet is never found in abyssal samples, unlike in xenoliths (e.g., Pearson et al., 2014), as the slow rate of emplacement of abyssal samples allows time for the breakdown of garnet to spinel and pyroxene. Low temperature amphiboles, such as tremolite, are found as an alteration phase in abyssal peridotites (Cannat and Seyler, 1995; Bach et al., 2004; Boschi et al., 2006). High temperature amphiboles, such as pargasite, have occasionally been identified in abyssal peridotites (Melson et al., 1967; Seyler et al., 2004) and occur in only 6 out of 1268 samples in this compilation. In contrast, some studies of xenoliths, ophiolites, and orogenic peridotites have suggested that pargasite is a ubiquitous trace phase in the mantle (e.g., Green, 1964; Niida and

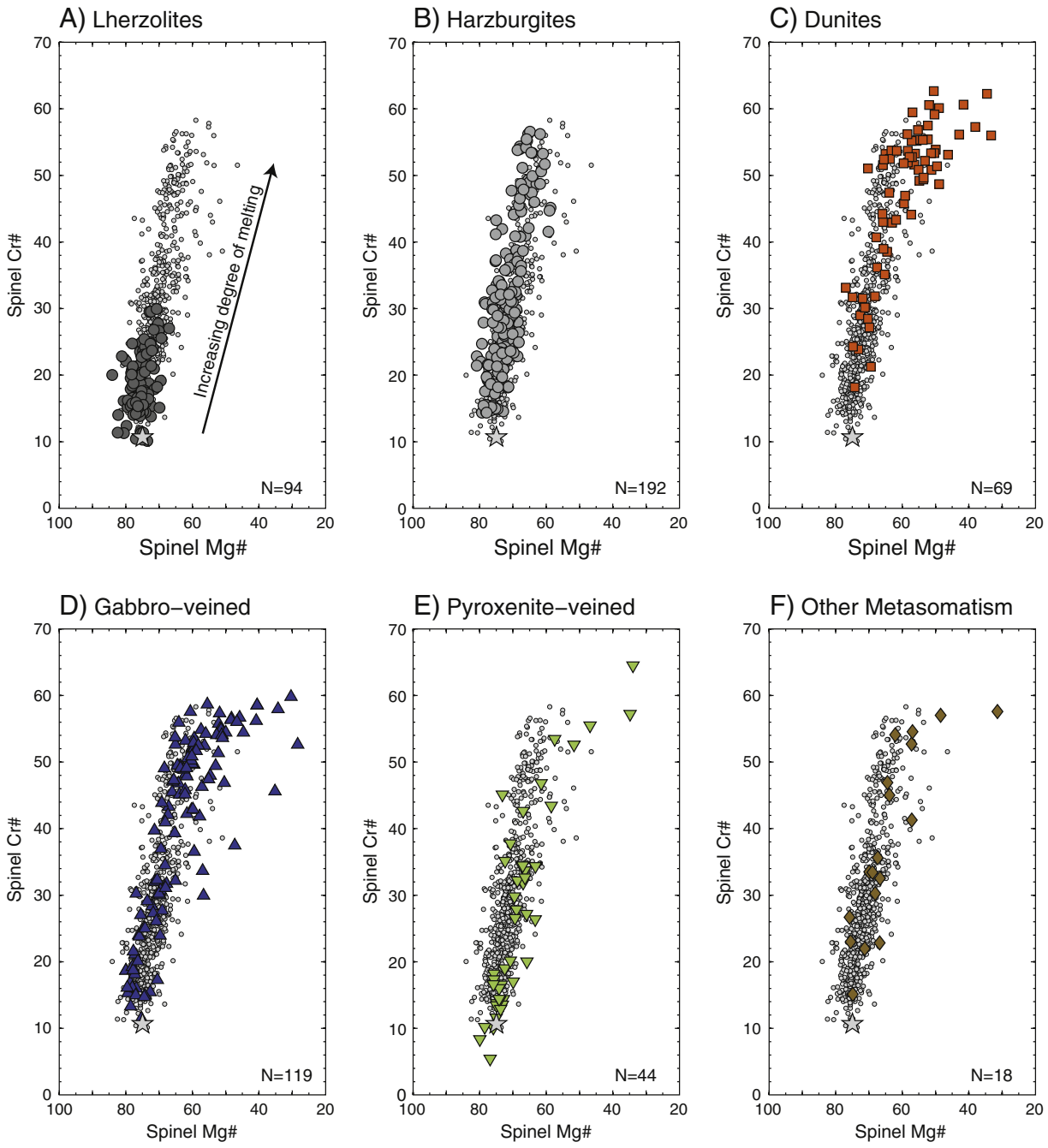

Fig. 5. Variation in spinel Cr# as a function of spinel Mg#. Spinel Cr# is plotted on an axis that is twice the length of the Mg# axis, as spinel contains two 3+ cations for every 2+ cation. The Mg# axis is reversed so that spinel shows a positive trend with increasing degree of melting. Residual peridotites are plotted as a background field of gray dots and the star represents model DM source composition (Workman and Hart, 2005). The background field consists of a larger dataset than the combined lherzolite and harzburgite datasets as many residual peridotites do not have accompanying modal data. All samples have Cr# in the range 10–60, except for a small number of dunites and pyroxenite-veined peridotites.

Green, 1999). The general lack of high temperature amphiboles in abyssal peridotites suggests that the oceanic mantle is relatively anhydrous. Estimates of upper mantle water content based on MORB water concentrations suggest that too little water is present for the mantle to contain pargasite (Hirschmann, 2006).

4.2. Mineral major element data

Major element data collected by electron microprobe and reported as wt.% oxides are provided for olivine, orthopyroxene, clinopyroxene, and spinel in Tables S1 and S2, as well as plagioclase in Table S2. Data were filtered to remove any analyses with wt% or cation totals that deviate by more than ±1.5% of a perfect total (e.g., outside the range 99.8–101.5% for wt.% totals, while cation totals should be 3, 4, or 5, depending on the mineral). In spinels, total iron is measured as FeO and then recalculated on the basis of stoichiometry to estimate the proportions of FeO and Fe_2O_3, following the methodology of Droop (1987).

Much of the discussion below for major elements focuses on spinel compositions (Figs. 5–6), which show the most systematic major element variations during melting (Dick and Bullen, 1984) and are the most resistant phase to alteration. Spinels are also not subject to the analytical uncertainty associated with pyroxenes, which have typically undergone extensive exsolution in abyssal peridotites. Many studies use a defocused electron beam and line traverses on pyroxenes to

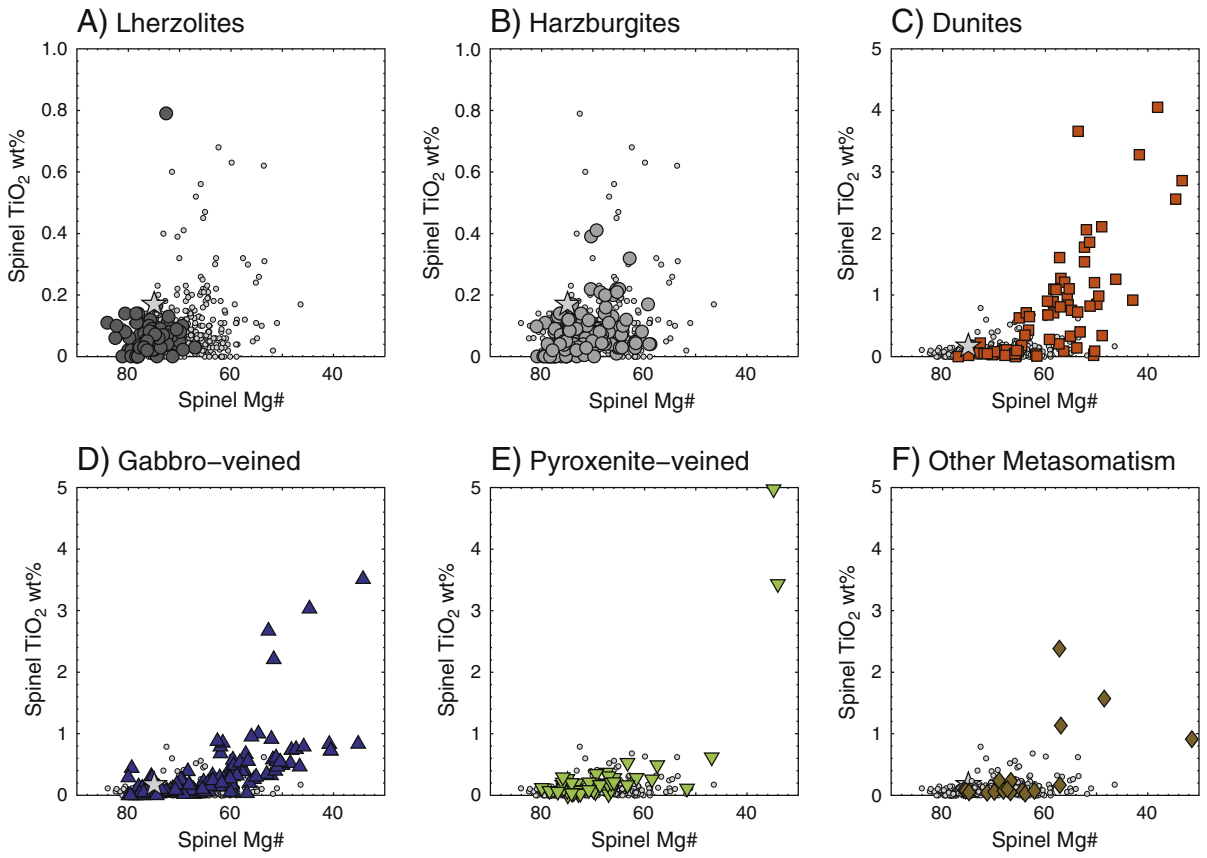

Fig. 6. Variation in spinel TiO_2 as a function of spinel Mg#, with the Mg# axis reversed for easier comparison to spinel data in Fig. 5. Residual peridotites are shown as a background field of gray dots and the star represents the model DM source composition from Workman and Hart (2005). Note the different scale for the TiO_2 axes in (A–B) compared to (C–F), as all lherzolites and harzburgites have $TiO_2 < 1$ wt.%.

average out the effects of exsolution to provide an estimate of the high temperature composition (e.g., Warren and Shimizu, 2010). Studies by Dick and co-workers through 1989 used hand-picked pyroxenes that were fused into glass prior to analysis to homogenize exsolution lamellae (Dick et al., 1984; Dick, 1989). This method provides more accurate compositions except for chromium, which can be lost if the fusion time is too long (Dick, 1989).

The compositional dataset for spinels is larger than for any other phase in the database, with >900 spinel analyses compared to ~450 for olivine. In particular, many dunites having only spinel compositional data and no modal or trace element data (Table S2). During melting, Cr# ($Cr/[Cr+Al]*100$) increases while Mg# ($Mg/[Mg+Fe^{2+}]*100$) decreases in spinel (Dick and Bullen, 1984), as shown in Fig. 5. Spinel Cr# varies from 10 to 60 among residual peridotites, with no ridge peridotites having Cr# > 60 (Fig. 5A–B), an observation originally made by Dick and Bullen (1984). For comparison, peridotites associated with subduction zones extend to Cr# = 85 (Dick and Bullen, 1984; Arai and Ishimaru, 2008). Lherzolite spinels have a maximum Cr# = 30 and minimum Mg# = 67, in agreement with their compositions reflecting limited degrees of melting. In contrast, harzburgite spinels cover the full spectrum of compositions, with Cr# = 14–57 and Mg# = 59–81.

Among veined samples, a few dunites and pyroxenites extend to Cr# > 60, but the majority plot within the same Cr# range as residual peridotites (Fig. 5). However, Mg# extends to lower values and TiO_2 concentration to higher values (up to 5 wt.%) than among residual peridotites (Fig. 6). Increased TiO_2 (Fig. 6) is often an indicator of re-equilibration with a melt (Dick and Bullen, 1984). Additionally, Ti enrichment in spinel occurs when plagioclase and olivine crystallize from a melt, as Ti is incompatible in these two minerals (Arai, 1992; Rampone et al., 1993; Khedr and Arai, 2010). A subset of "other metasomatized" peridotites were placed in this category on the basis of spinels with high (>1 wt.%) TiO_2 concentrations.

EPR peridotites always have spinel Cr# >30 (Fig. 7), which agrees with the presence of only harzburgites at the EPR (Fig. 4) corresponding to a high degree of melting. CIR, Arctic, and SWIR samples extend over most of the global range for spinel Cr#–Mg# (Fig. 7), in agreement with their mineral modal ranges (Fig. 4). However, variations in spinel Cr#–Mg# on a ridge basis do not always show the same pattern as variations in mineral modes. Samples from the AAR do not have spinel Cr# > 45, despite the presence of harzburgites in the modal dataset. The MAR consists mainly of harzburgites (75% of residual samples; Fig. 4), yet has an even distribution of peridotites across the full range of spinel Cr#–Mg#, with no weighting towards the harzburgite end of the spectrum (Fig. 7).

4.3. Clinopyroxene trace element data

Trace element data for clinopyroxene is included in Tables S1 and S2. When plotting abyssal peridotite data, mean CI chondrite (Anders and Grevesse, 1989) is usually used for normalization (Fig. 8). Most trace element datasets have been collected by secondary ion mass spectrometry (SIMS) (e.g., Johnson et al., 1990; Hellebrand et al., 2002a), but some recent studies have used laser ablation inductively coupled plasma mass spectrometry (LA-ICPMS) (e.g., Seyler et al., 2011; D'Errico et al., 2016). LA-ICPMS offers the advantage of faster collection times, but spot sizes are larger and elemental nterferences can be harder to detect. Improved instrumentation and the availability of a two-pyroxene trace element thermometer (Liang et al., 2013) have recently resulted in the analysis of orthopyroxene in addition to clinopyroxene

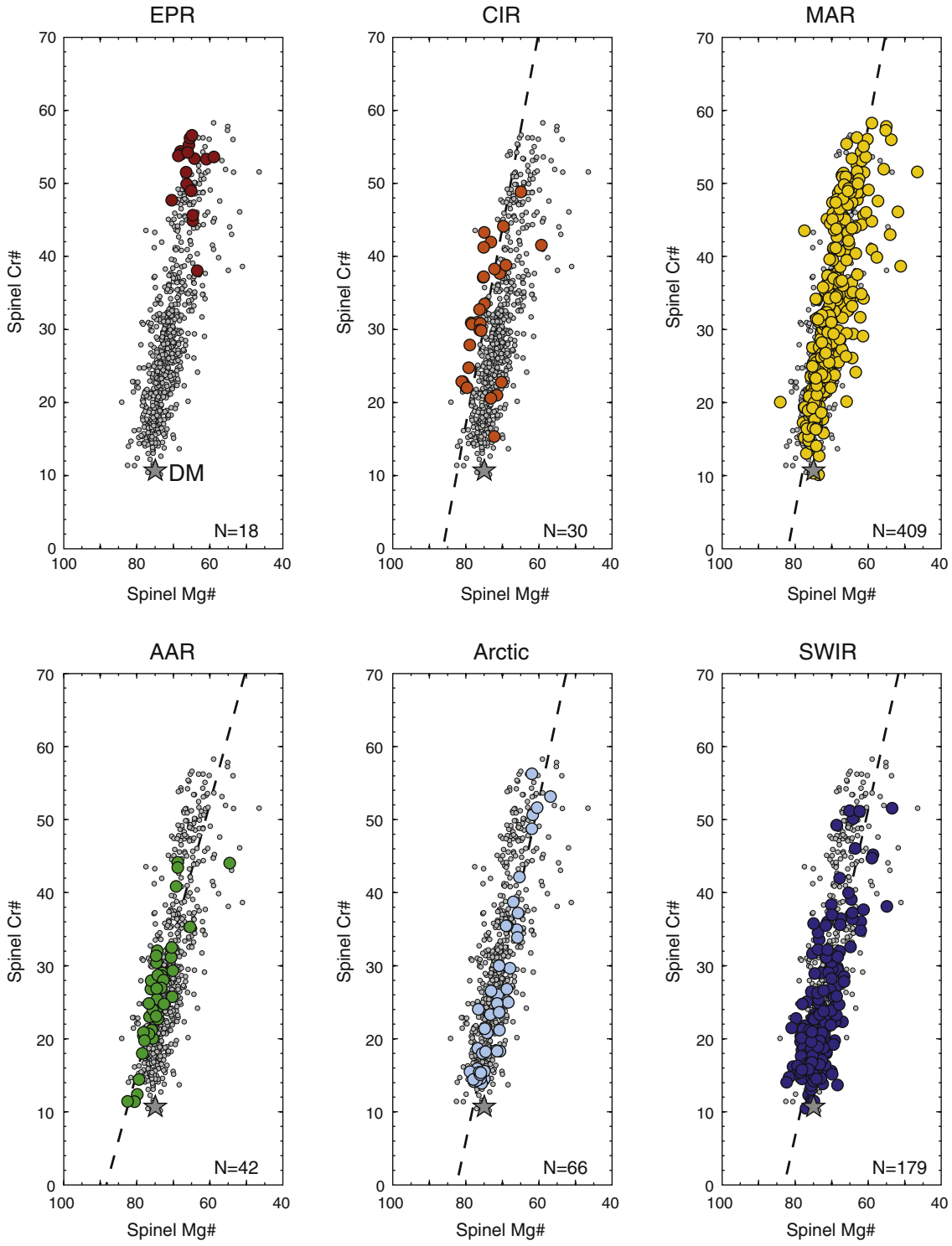

Fig. 7. Variation in spinel composition by ridge for residual peridotites. The gray symbols in the background are the global dataset for residual peridotites and the star indicates the model DM source composition. The maximum Cr# observed among all ridge peridotites is 60. Dashed lines are linear least squares regressions through each ridge dataset except for the EPR, where not enough data are available for a robust regression. Slight offsets among the regressions may reflect underlying compositional variability.

(Hellebrand et al., 2005; Warren et al., 2009; Brunelli and Seyler, 2010; Seyler et al., 2011; D'Errico et al., 2016), but this dataset is small and thus not included here.

Error analysis for SIMS data is discussed in detail by Hellebrand et al. (2002a) and Warren and Shimizu (2010) and for LA-ICPMS by (D'Errico et al., 2016). The error for trace element analyses can be large (>30%) due to the low concentration of many elements. However, high precision is often not necessary as concentrations vary on a log scale among elements and samples (Fig. 8). As a quality control in this compilation, analyses that do not have smoothly varying REE patterns have been excluded. A subset of samples across all peridotite categories have a "La-kick", with La concentrations enriched relative to Ce at low (<0.1 ppm) concentrations (Fig. 8). Whether this is an analytical artifact or a real aspect of the data is not adequately resolved. Many early datasets do not report La concentrations due to concerns over data quality (e.g., Johnson et al., 1990).

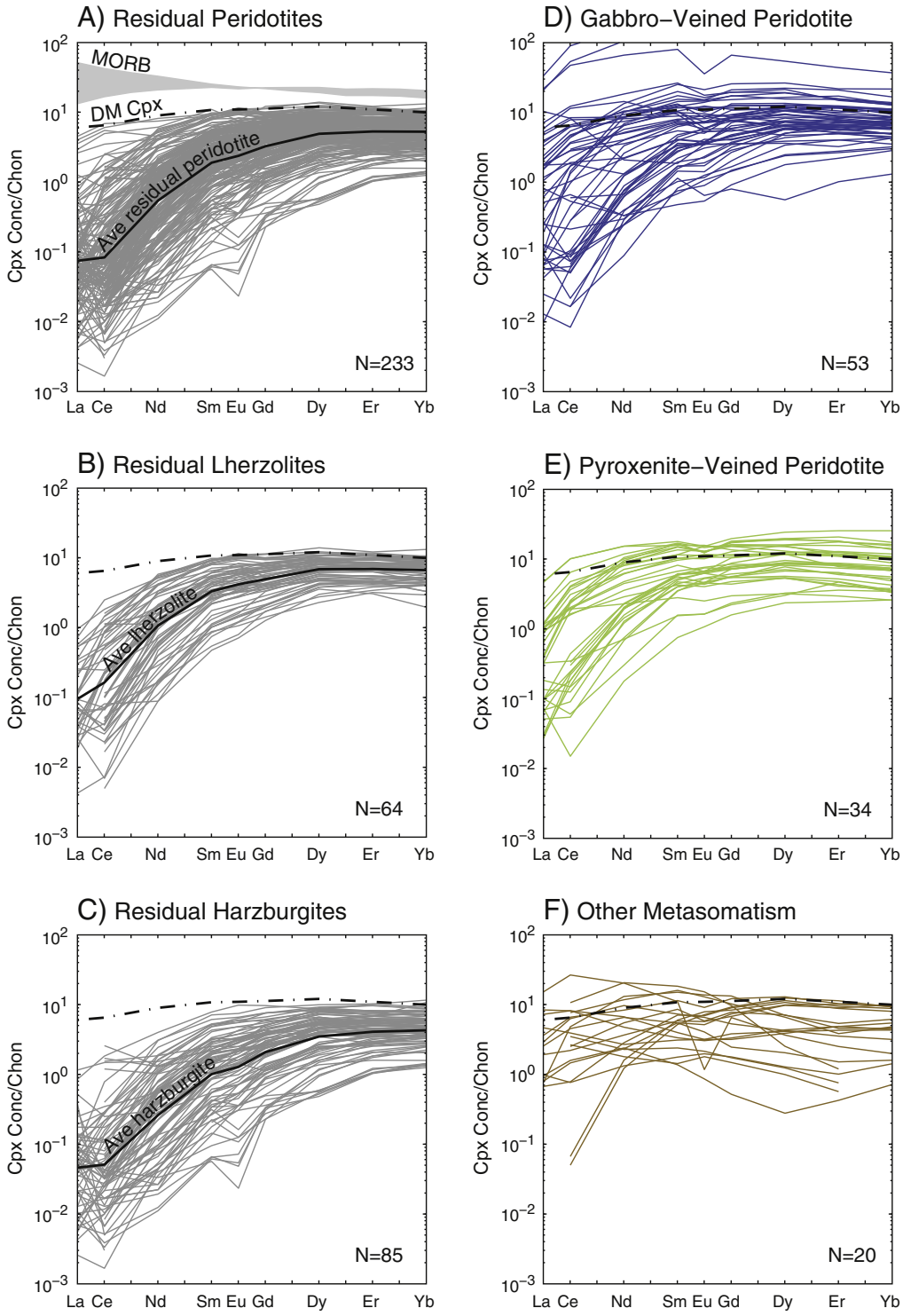

Fig. 8. REE concentrations in clinopyroxene plotted as a function of lithology. All data are in situ analyses of clinopyroxene normalized to chondrite (Anders and Grevesse, 1989). Also shown are MORBs (represented by the range of Depleted/Normal/Enriched MORB from Gale et al., 2013) and DM clinopyroxene (Workman and Hart, 2005). The number of residual peridotites in (A) is greater than the combined number of lherzolites (B) and harzburgites (C) as modal compositions have not been reported for all samples in the literature. Dunites are not shown as they rarely contain clinopyroxene and thus trace element data is only available for 3 samples.

Globally, abyssal peridotite REE concentrations range from relatively high – with concentrations similar to the model DM source – to very low. Lherzolites (Fig. 8B) do not extend to very low concentrations. Harzburgites range from the same concentrations as lherzolites down to very low concentrations (Fig. 8C), suggesting the susceptibility of clinopyroxene at low modal abundances to melt–rock interaction. Veined peridotites have relatively fertile compositions, particularly among gabbro-veined peridotites (Fig. 8D). Some of the peridotites in the "other metasomatized" category have $LREE_N > HREE_N$ (Fig. 8F), which is one of the criteria used to classify peridotites into this group. In hand sample, these peridotites contain no obvious characteristics, such as veins, to indicate melt–rock interaction. However, trace element modeling (discussed further below) indicates that $LREE_N > HREE_N$ can only be reproduced by interaction with small amounts of melt (Hellebrand et al., 2002a; Brunelli et al., 2014; D'Errico et al., 2016).

The REE composition of residual peridotites is plotted by ridge in Fig. 9. EPR harzburgites again have very refractory compositions, though the dataset is limited to 6 samples from Hess Deep. The samples contain cross-cutting gabbro veins and many of the REE patterns have negative Eu anomalies (Dick and Natland, 1996), which implies plagioclase crystallization. The infertility of Hess Deep harzburgites, despite their proximity to melt veins, supports the interpretation of high degrees of melting at this fast spreading ridge (e.g., Niu and Hékinian, 1997b). Peridotites extend over large compositional ranges at the MAR, Arctic ridges, and SWIR, with LREE variations of 2–3 orders of magnitude and HREE variations of 1 order of magnitude. The abundance of harzburgites at the MAR does not correspond to notably lower trace element concentrations. Gakkel Ridge peridotites do not extend to very low concentrations, but many Gakkel harzburgites are clinopyroxene-free and have orthopyroxenes with low trace element concentrations (D'Errico et al., 2016). Overall, peridotites from slow

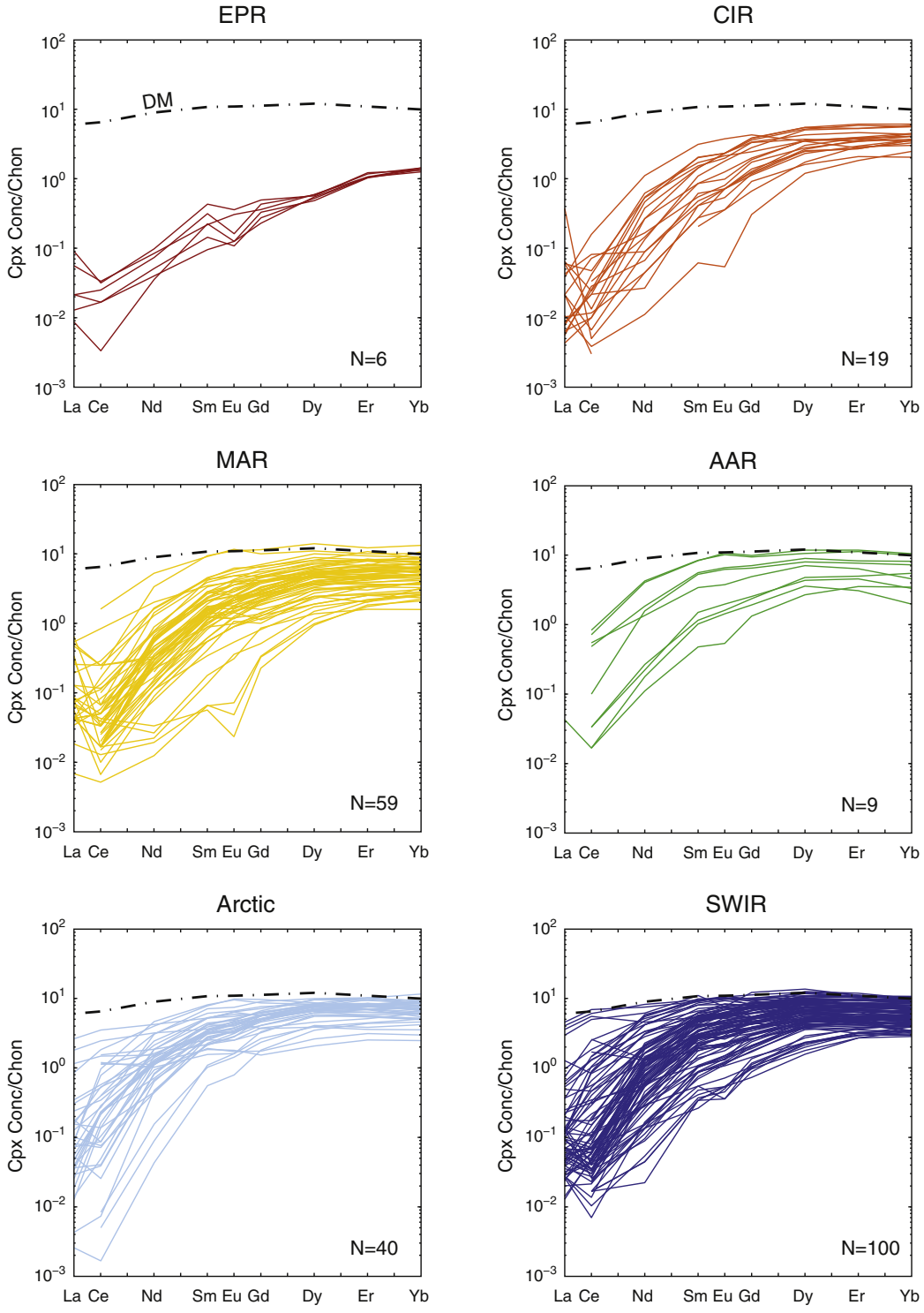

Fig. 9. Variations in clinopyroxene REE concentrations plotted by ridge for residual peridotites only. All data are in situ analyses of clinopyroxene, normalized to chondrite (Anders and Grevesse, 1989). The dot-dashed line is the DM composition of clinopyroxene from Workman and Hart (2005).

and ultraslow spreading ridges cover a large compositional range, despite models that predict reduced degrees of melting due to on-axis conductive cooling (e.g., Bown and White, 1994; Sleep and Barth, 1997).

5. Discussion

5.1. Compositional variations as a function of spreading rate

Abyssal peridotites – both veined and unveined – cover large compositional ranges for mineral modes (Fig. 3), major elements (Figs. 5–6), and trace elements (Fig. 8). An obvious explanation for this variability is that it reflects variations in degree of melting. However, this alone cannot explain the compositional scatter among abyssal peridotites, as demonstrated by plotting the compositional range of residual peridotites as a function of spreading rate (Fig. 10). Two features are evident: (1) the amount of variation is greater at slow and ultra-slow spreading ridges than at fast spreading ridges (with the caveat that the dataset for fast spreading ridges is small) and (2) infertile peridotites (indicated by low modal clinopyroxene, high spinel Cr#, and low Yb in clinopyroxene) occur at all ridges, independent of spreading rate.

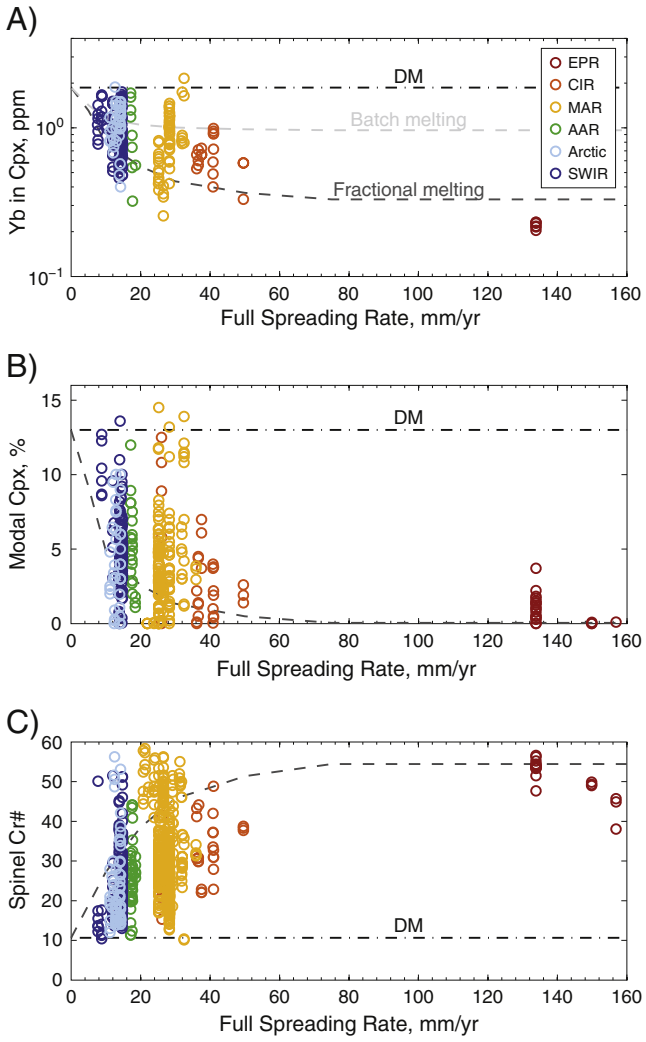

Fig. 10. Variation in residual peridotite compositions as a function of spreading rate for (A) Yb in clinopyroxene, (B) modal clinopyroxene, and (C) spinel Cr#. The dot-dashed lines indicate the model DM source composition (Workman and Hart, 2005) and the dashed lines are predicted variations due to melting. The degree of melting was determined as a function of spreading rate from the melt generation model of Bown and White (1994). This model predicts a decrease in F from 18% to 6% as the full spreading rate decreases from 160 mm/yr to 6 mm/yr, due to the effect of conductive cooling at low spreading rates. The fractional melting model (dark gray dashed lines) is shown in all panels and batch melting (light gray dashed line) is also shown in (A). The calculations in (A) and (B) use the reference model parameters described in the text. In (C), the variation of spinel Cr# as a function of F is based on the empirical calibration $F = 9 * \ln(\text{Cr}\#) + 23$ (for Cr# in decimal units), which is derived from the relationship between spinel Cr# and clinopyroxene Yb (e.g., Hellebrand et al., 2001).

The compositional range of residual peridotites does not match predictions based on variations in degree of melting (F) as a function of spreading rate. To first order, F at ridges should be uniform as upwelling mantle will cross the solidus at the same depth, regardless of spreading rate. However, at full spreading rates <40 mm/yr, conductive cooling limits the height of the melting column from above, resulting in the formation of thinner basaltic crust (Bown and White, 1994; Niu and Hékinian, 1997b; Sleep and Barth, 1997; Dick et al., 2003; Montési and Behn, 2007; Sleep and Warren, 2014). To provide an estimate for this effect on mantle melting, Fig. 10 shows the predicted variation in peridotite composition based on the Bown and White (1994) melting model for the influence of conductive cooling on melt generation. Modal clinopyroxene and Yb in clinopyroxene were calculated by combining this estimate for F as a function of spreading rate with a nonmodal fractional melting model, the details of which are discussed in the next section. This model does not reproduce the most depleted compositions (e.g., EPR peridotites), but adjusting model parameters or using a more sophisticated melting model does not provide a fit through all data points. This modeling does not take into account estimates for mantle potential temperature variations based on seismic crustal thickness estimates, ridge depths, and basalt compositions (e.g., Klein and Langmuir, 1987; Dalton et al., 2014), which would cause variations in F independent of spreading rate.

The spread in residual peridotite compositions as a function of spreading rate suggests that (1) parts of the upper mantle have undergone previous cycles of melt removal, and (2) melt–rock interaction is an important process in the lithospheric mantle at ridges. In the following sections, I assess the role of these mechanisms in the generation of oceanic lithosphere, after first reviewing estimates for degree of melting in peridotites.

5.2. Estimating degree of melting

The composition of abyssal peridotites can be used to estimate the degree of melting that has occurred to produce oceanic crust. The simplest way to estimate F is to model trace element abundances assuming fractional melting, which Johnson et al. (1990) showed provides a better fit for abyssal peridotites than batch melting. Within this framework, any variation in MORB or peridotite composition is interpreted as representing a variation in degree of melting at the ridge. This interpretation relies on two key assumptions: (1) the peridotite has not undergone any process apart from melting and instantaneous melt removal and (2) the source mantle has a uniform composition. Studies of peridotites and MORBs have shown that neither assumption is valid (e.g., Hirschmann and Stolper, 1996; Seyler et al., 2001; Hellebrand et al., 2002a; Brunelli et al., 2006; Warren et al., 2009; Stracke et al., 2011; Lambart et al., 2013; Gale et al., 2014), as will be discussed in the next two sections. However, fractional melt modeling provides a first step in unraveling the processes recorded in abyssal peridotites, providing an estimate for F that can be compared to other estimates, such as those derived from basalt chemistry or seismic refraction estimates of crustal thickness (e.g., Klein and Langmuir, 1987; Forsyth, 1993; Bown and White, 1994; White et al., 2001). The focus here for modeling is to reproduce HREE abundances, as LREE abundances are more influenced by melt–rock interaction (discussed in the next section).

5.2.1. Fractional melting model

Equations for the evolution of the concentration (C_s^i) of trace element i in the bulk residue (s) as a function of degree of melting (F) were developed by Gast (1968) and Shaw (1970). For nonmodal

fractional melting, the equation is:

$$\frac{C_s^i}{C_0^i} = \left(\frac{1}{1-F}\right)\left(1-\frac{PF}{D_0^i}\right)^{\frac{1}{P}} \quad (1)$$

where C_0^i is the initial concentration and D_0^i is the initial bulk solid partition coefficient for element i. P is the weighted partition coefficient:

$$P = \sum p_\alpha D_\alpha^i = p_{oliv}D_{oliv}^i + p_{opx}D_{opx}^i + p_{cpx}D_{cpx}^i + p_{spin}D_{spin}^i \quad (2)$$

where D_α^i is the mineral/melt partition coefficient for phase α. The variable p_α is the proportion of each mineral phase entering the melt, hence p_α corresponds to the coefficients in the melting reaction.

Abyssal peridotite trace element datasets are based on clinopyroxene trace element abundances, while the above equations use abundances in bulk peridotite. Eq. (1) can be recast in terms of the variation in clinopyroxene trace element concentration (C_{cpx}^i), as derived by Johnson et al. (1990):

$$\frac{C_{cpx}^i}{C_{0,cpx}^i} = \left(1-\frac{PF}{D_0^i}\right)^{\left(\frac{1}{P}-1\right)}. \quad (3)$$

Additionally, to convert between bulk and clinopyroxene trace element concentrations, the following two equations are used:

$$C_{bulk}^i = C_{cpx}^i\left(\frac{D_{bulk}}{D_{cpx}}\right) \quad (4)$$

$$D_{bulk} = \sum x_\alpha D_\alpha^i = x_{oliv}D_{oliv}^i + x_{opx}D_{opx}^i + x_{cpx}D_{cpx}^i + x_{cpx}D_{cpx}^i + x_{spin}D_{spin}^i \quad (5)$$

where x_α is the mineral mode.

The fractional melting model is provided as a MatLab m-file in the supplemental material. The standard ways to plot the results of melt modeling are chondrite-normalized REE plots (Fig. 11) and $(Sm/Yb)_N$ versus Yb_N in clinopyroxene (Fig. 12). The latter type of plot allows comparison of different model runs, whereas the former provides a better indication of the overall model fit. Most published models show results of melting calculations by plotting either clinopyroxene or bulk REE abundances, but not both. However, the model fit for clinopyroxene versus bulk rock trace elements is not always equally good, as shown by comparing the two plots in Fig. 11.

5.2.2. Model parameters

Melt modeling requires constraints on: (i) source composition, (ii) mineral/melt partition coefficients, and (iii) melting reactions. The effect of these different parameters on model outcome is compared in Fig. 12 and discussed in this section. Results of different model runs are compared to a reference model (Fig. 11, parameters given in caption), which is represented by the black dashed line in Fig. 12. Among the parameters, initial clinopyroxene mode and partition coefficients have the most significant effect on trace element abundances as a function of F (Fig. 12).

5.2.2.1. Source composition. Many studies use the initial trace element and modal composition of the source given in Johnson et al. (1990). This estimate for mantle composition is based on trace element concentrations from a LREE-depleted lherzolite (Loubet et al., 1975) and mineral modes calculated for peritectic melting of spinel peridotite. Subsequent studies replaced these mineral modes with estimates for the mantle source from Hart and Zindler (1986). More recent models, including the one shown in Fig. 11, use estimates for DM composition based on global compilations of MORB and abyssal peridotite compositions (Salters and Stracke, 2004; Workman and Hart, 2005). Spinel is usually ignored in REE models dues to its low modal abundance in the source and melting reaction, combined with the extreme incompatibility of most trace elements in spinel.

Among all the variables in melting models, initial clinopyroxene mode has the largest effect on the trajectory of trace element abundances, with the difference in predicted F growing increasingly larger as melting proceeds (Fig. 12). Initial mantle with 17% clinopyroxene (green line in Fig. 12) evolves more rapidly to lower trace element abundances than mantle with 13% clinopyroxene (all other lines in Fig. 12), which can result in a difference of >5% in the estimate of F for a given composition. Clinopyroxene-out is not reached until ~24% melting when the initial mode is 17% (the early estimate for clinopyroxene mode in DM, from Johnson et al., 1990), whereas clinopyroxene-out occurs at ~18% melting for an initial 13% clinopyroxene (current estimate for clinopyroxene mode, from Workman and Hart, 2005).

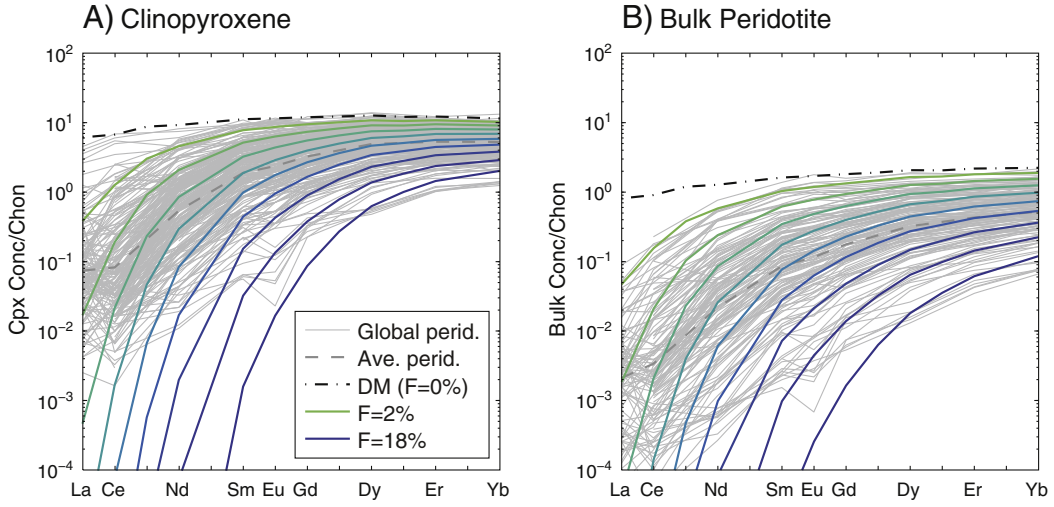

Fig. 11. Nonmodal fractional melting model for REE in (A) clinopyroxene and (B) bulk peridotite in increments of 2% melting. For comparison, residual abyssal peridotites (thin gray lines = individual samples; dashed gray line = average) are shown, with bulk peridotite concentrations calculated from clinopyroxene concentrations using Eqs. (4)–(5). The melting model uses a DM starting composition (black dot-dashed line; Workman and Hart (2005)), partition coefficients calculated for mantle with a DM composition at a potential temperature of 1300 °C (Table S3; Sun, pers. comm. 2014; Sun and Liang, 2014) and the melting reaction for DMM1 composition at 1.0 GPa: $0.56Opx + 0.72Cpx + 0.04Spin = 0.34Oliv + 1Melt$ (Wasylenki et al., 2003).

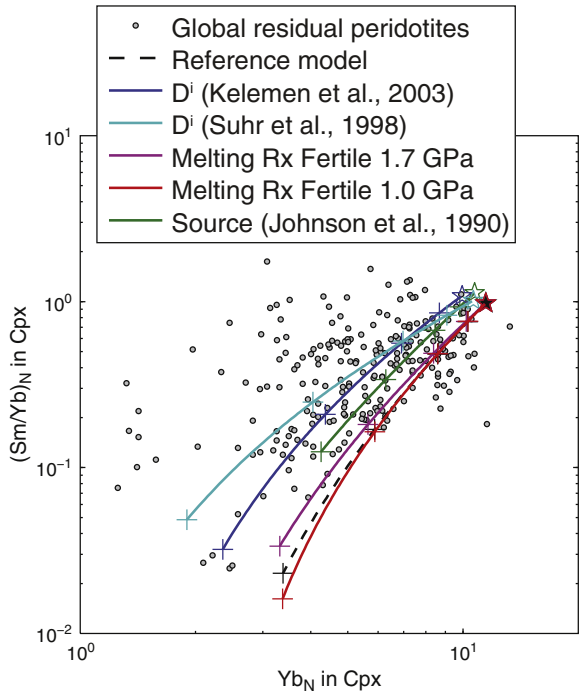

Fig. 12. Comparison of fractional melting model parameters, shown as the variation of $(Sm/Yb)_N$ as a function of Yb_N, both in clinopyroxene. The reference model (black dashed line) is calculated using the same parameters as in Fig. 11. The two D^i models compare partition coefficients from Kelemen et al. (2003) and Suhr et al. (1998) to the Sun and Liang (2014) partition coefficients in the reference model. The melting reaction is compared for the 1.7 GPa reaction of fertile peridotite (Kinzler, 1997) and the 1.0 GPa reaction of FER-E (Pickering-Witter and Johnston, 2000) to the reaction in the reference model at 1.0 GPa for DMM1 (Wasylenki et al., 2003). The source model compares the composition used by Johnson et al. (1990, with 17% clinopyroxene) to the reference model (DM with 13% clinopyroxene, based on Workman and Hart, 2005). Stars indicate the starting composition for each model and crosses show increments of 2%, 5%, 10%, and 15% melting, with melting truncated at 15% melting for easier comparison between models.

5.2.2.2. Partition coefficients. Mineral/melt partition coefficients are constrained from studies of experiments and natural samples. The main REE partition coefficient datasets (Suhr et al., 1998; Kelemen et al., 2003; Sun and Liang, 2014) used in abyssal peridotite models are given in Table S3. Most studies have used either the compilation by Kelemen et al. (1993, 2003) or by Suhr et al. (1998), both of which are based on Hart and Dunn (1993) for REE partitioning between clinopyroxene and basaltic melt. Suhr et al. (1998) adjusted Yb partition coefficients to lower values, but did not provide a reason for revising these values.

More recently, Sun and Liang presented equations for calculating REE partition coefficients between mantle minerals and basaltic melts using a parameterized lattice strain model calibrated against a large database of partitioning experiments (Sun and Liang, 2012, 2013a,b, 2014; Yao et al., 2012; Liang et al., 2013). This model allows partition coefficients to be calculated as a function of mineral composition, temperature and pressure. As demonstrated by Sun and Liang (2014), their updated set of partition coefficients provides a better fit to partitioning measurements made in well-equilibrated peridotite xenoliths compared to previous partition coefficients. The Sun and Liang (2014) mineral–melt partition coefficients provided in Table S3 were calculated by Sun (pers. comm. 2014) for mantle with a DM composition at a potential temperature of 1300 °C.

The effect of using the Sun and Liang (2014) partition coefficients compared to the previous compilations (Suhr et al., 1998; Kelemen et al., 2003) is to produce a smoother REE pattern and higher REE concentrations for a given degree of melting (Fig. 12). The divergence between calculated concentrations increases with increasing degree of melting, such that, at $F = 15$ %, clinopyroxene $Yb_N = 4.0$ for values of D^i_α from (Sun and Liang, 2014), compared to $Yb_N = 2.8$ for D^i_α from (Kelemen et al., 2003) and $Yb_N = 2.2$ for D^i_α from Suhr et al. (1998).

5.2.2.3. Melting reaction. Many abyssal peridotite studies (e.g., Hellebrand et al., 2002a; Brunelli et al., 2006; Warren and Hauri, 2014) use the melting reaction from Kinzler (1997) for melting of fertile mantle at 1.7 GPa: $0.28Opx + 0.67Cpx + 0.11Spin = 0.06Oliv + 1Melt$. As pressure decreases, the amount of pyroxene consumed and olivine produced increase, such that the reaction at 1.0 GPa is: $0.56Opx + 0.72Cpx + 0.04Spin = 0.34Oliv + 1Melt$ (Wasylenki et al., 2003). This 1 GPa reaction is used for the reference model (Figs. 11–12), because Walter (2014) found that abyssal peridotite major element compositions are successfully modeled with an average pressure of 1 GPa. In addition, melting reaction coefficients have been measured for the largest range of compositions at 1 GPa (e.g., Kinzler, 1997; Robinson et al., 1998; Walter, 1998; Walter, 2014; Longhi, 2002). Varying the pressure of melting has a relatively minor effect on the trajectory of the melting model (Fig. 12). The purple line for melting at 1.7 GPa (fertile mantle melting; Kinzler, 1997) is only slightly offset from the black dashed line (reference model) and the red line (fertile mantle melting; Pickering-Witter and Johnston, 2000), which are both for melting at 1.0 GPa.

Source fertility also influences the melting reaction, with the amount of orthopyroxene consumed and olivine produced increasing with decreasing mantle fertility (i.e., as modal clinopyroxene and alkalis in the source decrease; Wasylenki et al., 2003). However, this effect is relatively minor, as shown by comparison of the reference model (black dashed line; DMM1 composition of Wasylenki et al., 2003) to more fertile compositions at 1.0 GPa (red line; FER-E composition of Pickering-Witter and Johnston, 2000) and 1.7 GPa (purple line; fertile peridotite composition of Kinzler, 1997). The reaction of Wasylenki et al. (2003) is used for the reference model, because these experiments used a starting composition (DMM1) that is similar to the model DM source. A more rigorous implementation of the melting model would allow the melting reaction to vary as a function of changing pressure and mantle fertility, for example by incorporating the recent parameterization of Behn and Grove (2015).

5.2.3. Model fit and implications

The nonmodal fractional melting model in Fig. 11 provides a first order fit to the REE patterns of global abyssal peridotites, with a better fit for HREEs than LREEs. This model makes several simplifications, including the use of constant partition coefficients and a constant melting reaction, whereas both evolve as a function of pressure, temperature, and composition. Source composition is assumed to be represented by DM, though observations from MORBs and peridotites indicate that mantle composition can deviate significantly from this model composition (e.g., Seyler et al., 2003; Brandon et al., 2000; Harvey et al., 2006; Warren et al., 2009; Dalton et al., 2014; Gale et al., 2014). Fractional melting predicts that LREEs should be absent from peridotites by ~15% melting, yet they always have detectable concentrations in peridotites (Fig. 8). Enrichments in LREEs have been suggested to result from various types of melt–rock interaction (e.g., Brunelli et al., 2006; Seyler et al., 2007; Godard et al., 2008; Warren et al., 2009). More sophisticated models that include melt transport effects (e.g., Vernières et al., 1997; Spiegelman and Kelemen, 2003; Liang and Parmentier, 2010; Katz and Weatherley, 2012; Brunelli et al., 2014) are discussed in the next section. Despite the simplifications of the nonmodal fractional melting model, the range in F of ~2–18% is in reasonable agreement with estimates based on MORB geochemistry (8–15%; Salters and Stracke, 2004) and abyssal peridotite major elements (2–25%; Walter, 2014).

The largest simplification in the melting model is the exclusion of garnet-field melting. MORB trace element and isotope geochemistry indicate that melting begins in the garnet stability field, though

garnet pyroxenites are estimated to be the main source of melt at these depths (Hirschmann and Stolper, 1996). As discussed by Hellebrand et al. (2002a), the overall effect of incorporating garnet-field melting is to produce lower ratios of $LREE_N/HREE_N$ in clinopyroxene (e.g., Sm_N/Yb_N in Fig. 12) due to the compatibility of HREE in garnet. However, Fig. 12 shows that varying the model parameters for spinel-field melting alone can produce melting trajectories with low Sm_N/Yb_N. This conclusion was also reached by Hellebrand et al. (2002a), who suggested that source mantle with a low clinopyroxene mode, but high REE abundances, will melt to produce a residue with low Sm_N/Yb_N. As many harzburgites in the abyssal peridotite database match this description – particularly samples from the MAR – low $LREE_N/HREE_N$ ratios may also reflect variability in source composition.

Studies that have included garnet-field melting in trace element models yield estimates of ~3% to >10% melting in the garnet field (e.g., Johnson et al., 1990; Hellebrand et al., 2002a; Brunelli et al., 2006; Mallick et al., 2015). These estimates are relatively high given that mantle upwelling beneath ridges intersects the dry peridotite solidus close to the garnet-to-spinel transition, around 60 km depth, and that deeper hydrous peridotite melting is estimated to be low volume based on the low water content of the mantle (Hirschmann et al., 2009). In addition, the total amount of melting estimated in many trace element models is often high (>20%) relative to the amount required to produce average oceanic crustal thicknesses of ~6 km from mantle with a DM composition (e.g., White et al., 1992; Forsyth, 1993; Hirschmann and Stolper, 1996). Given the uncertainties in model parameters, more detailed testing needs to be done of abyssal peridotite trace element compositions to explore the trade-off between source composition and garnet-field melting. In addition, existing models – including the one presented above – do not reproduce the subset of peridotites with high Sm_N/Yb_N (Fig. 12). These high ratios may reflect melting of source material with high initial clinopyroxene mode (e.g., pyroxenite).

The effect of subsolidus re-equilibration in re-distributing trace elements between clinopyroxene and other minerals is not included in the above modeling. Subsolidus processes, particularly the exsolution of orthopyroxene from clinopyroxene and vice versa, are important in abyssal peridotites due to their slow ascent to the seafloor. Recently, Sun and Liang (2014) modeled REE subsolidus exchange between clinopyroxene and other minerals using their parameterization of mineral–mineral partition coefficients as a function of temperature. They found that clinopyroxene HREE abundances increase during exsolution, with a greater increase in abundance when clinopyroxene modal abundance is lower (i.e., harzburgitic clinopyroxene is more affected by subsolidus re-equilibration than lherzolitic clinopyroxene). As subsolidus re-equilibration results in lower Sm_N/Yb_N ratios, this effect moves peridotite compositions in the same direction as garnet-field melting (Sun and Liang, 2014). In addition, the increase in clinopyroxene REE concentrations during subsolidus re-equilibration means that F is under-estimated unless subsolidus re-equilibration is corrected for prior to modeling F.

The three main parameters of peridotite fertility (modal clinopyroxene, spinel Cr#, and clinopyroxene trace elements) are variably correlated (Fig. 13). HREE and Cr# have the strongest correlation, with a correlation coefficient of −0.76 between Yb_N and Cr# (Fig. 13A). This correlation has been used to derive an empirical relationship for F as a function of spinel Cr# (Batanova et al., 1998; Hellebrand et al., 2001). Using a fractional melting model, Hellebrand et al. (2001) determined the relationship $F = 10 * \ln(\text{Cr\#}) + 24$, for F in percent and Cr# in decimal units (Fig. 13D). Using the reference set of parameters for the fractional melting model above to calculate F for each Yb concentration in the global dataset, followed by regression of these values against spinel Cr#, gives the slightly modified relationship: $F = 9 * \ln(\text{Cr\#}) + 23$ (also for F in percent and Cr# in decimal units; Fig. 13D). However, the relationship between Cr# and Yb is subject to considerable scatter as these two parameters are not always coupled in abyssal peridotites (Fig. 13A). Some individual dredges and even individual peridotites can have large ranges of spinel Cr# (Hellebrand et al., 2002a), which cannot reflect variation in adiabatic decompression melting alone at such small spatial scales. Some of this local-scale heterogeneity may reflect melt–rock interaction, as has been observed near dunite channels in orogenic peridotites (Suhr et al., 2003; Morgan et al., 2008). Hence, assumptions must be made in identifying a representative spinel composition for a given location — for example, by averaging Cr# on a dredge basis (Zhou and Dick, 2013).

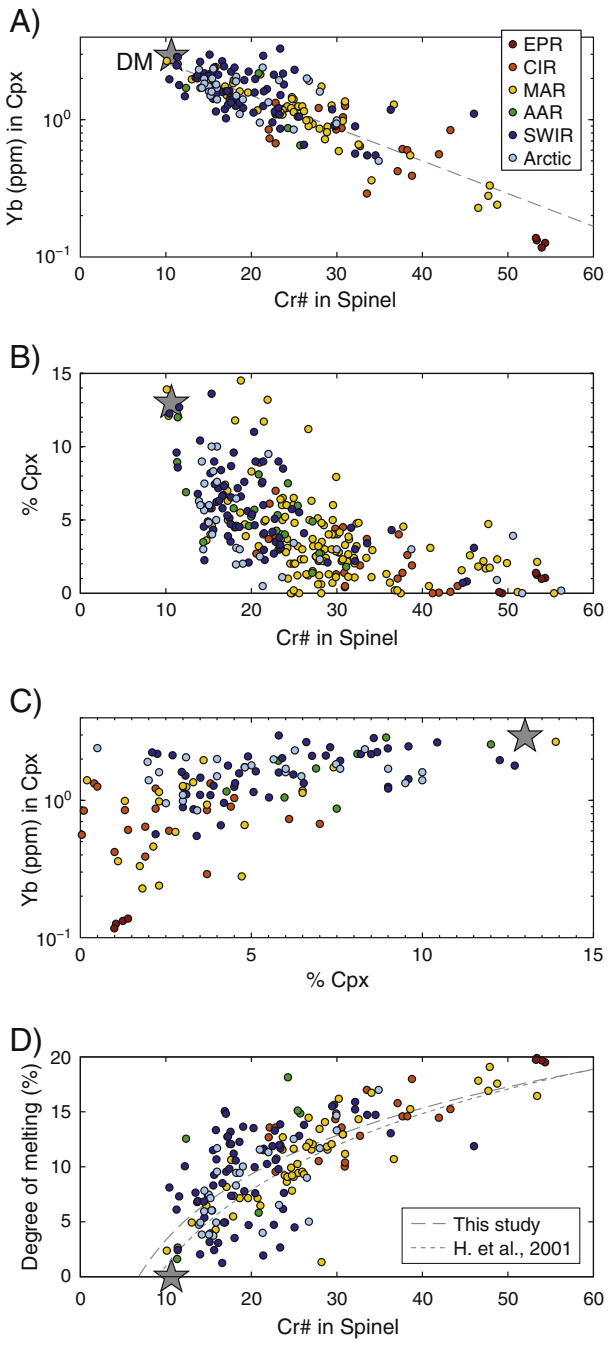

Fig. 13. (A–C) Co-variation of the three main proxies for degree of melting in peridotite: modal clinopyroxene, spinel Cr#, and Yb in clinopyroxene. The gray line in (A) indicates the regression of Yb against Cr#, which has a coefficient of correlation of −0.76. (D) Empirical calibration for degree of melting based on the relationship between spinel Cr# and Yb in clinopyroxene, derived by modeling Yb using fractional melting and regressing these values for F against spinel Cr#. The gray dashed lines are the relationships determined in this study and in Hellebrand et al. (2001).

5.3. Melt–rock interaction

Fractional melting is an end-member scenario for the generation of melts at mid-ocean ridges and provides a first-order fit to the trace element composition of abyssal peridotites. However, studies of major and trace elements in abyssal peridotites have also proposed that melts interact with the mantle during their extraction (e.g., Kelemen et al., 1992, 1997; Asimow, 1999; Lambart et al., 2012; Brunelli et al., 2014). Studies of U-series disequilibria in MORBs suggest that melt transport occurs in channels that allow high melt fluxes (e.g., Rubin and Macdougall, 1988; Elliott and Spiegelman, 2003). Theoretical and experimental models show that reactive infiltration instability can lead to the formation of channels in the partially molten mantle beneath ridges (e.g., Daines and Kohlstedt, 1994; Aharonov et al., 1995; Liang et al., 2010; Katz and Weatherley, 2012). Kelemen et al. (1995) argued that the dunite bodies exposed in ophiolites represent the channels by which the majority of melt is removed from the shallow mantle, through the reaction of deep, low-degree melts with shallow residues of higher degrees of melting. This model provides an interpretation for abyssal dunites, which are present in many ultramafic dredges (Fig. 1B) and correspond to at least 6% of abyssal ultramafic samples.

In detail, peridotite compositions cannot be completely matched by fractional melting models (Figs. 11–12), as abundances of highly incompatible elements are too high compared to moderately incompatible elements and clinopyroxene modes (e.g., Asimow, 1999). For example, in Fig. 14, the lowest Ce concentrations imply only 8% melting, whereas the lowest Yb concentrations require at least 18% melting. In addition to the formation of dunites, the migration of melts through the mantle results in other forms of melt–rock interaction, examples of which include gabbro and pyroxenite veins in abyssal peridotites. The term *melt–rock interaction* is used here to encompass a range of processes, from simple melt crystallization with decreasing temperature to open-system melting, where the host peridotite is both melting and reacting with a migrating melt. Melt–rock interaction in this general definition refers to situations where the melt-mass is increasing (a melting process), where melt-mass is decreasing (a solidification process), or where melt-mass is constant (a re-equilibration process). Hence, this

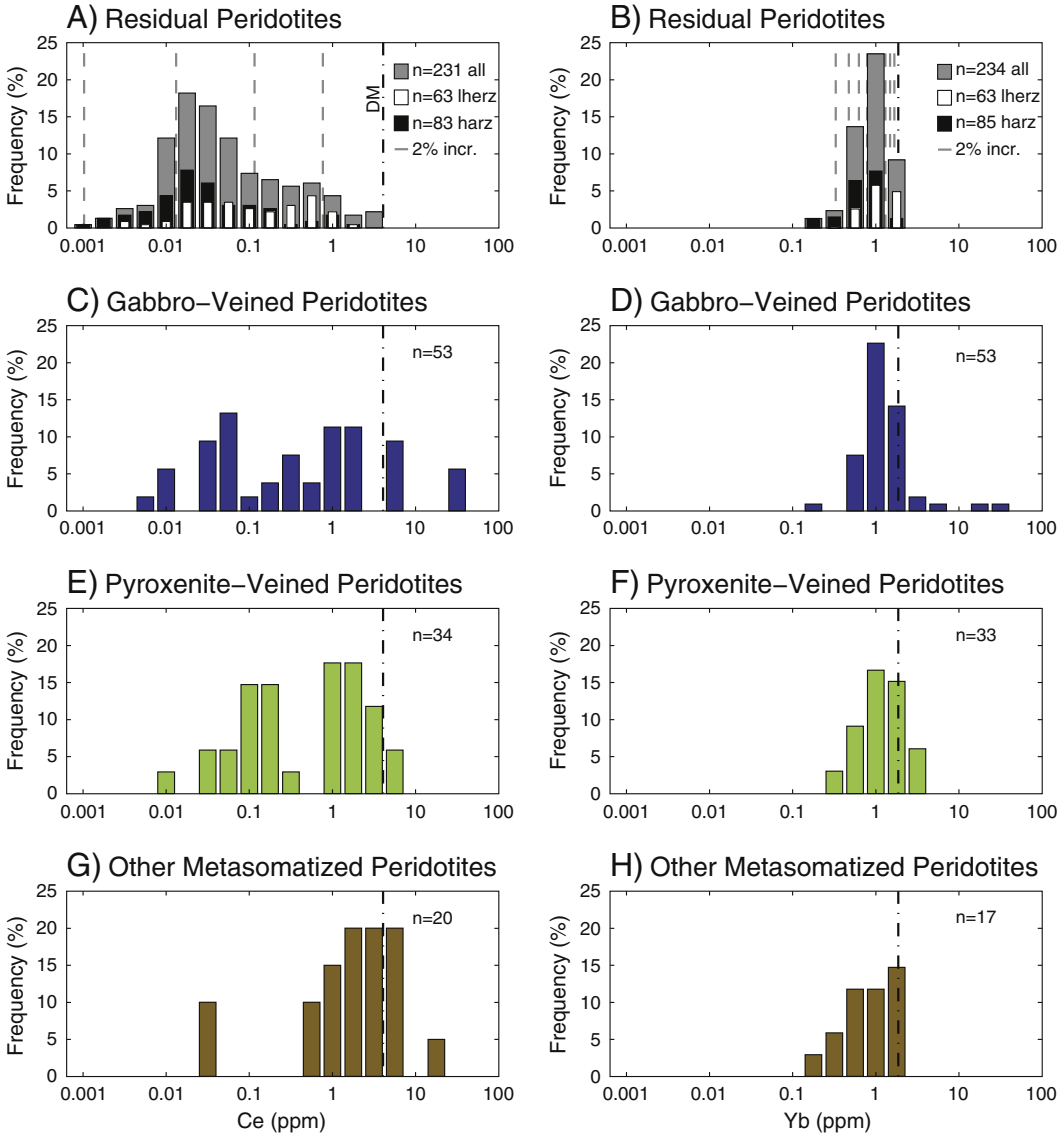

Fig. 14. Histograms of Ce and Yb concentrations in peridotite clinopyroxenes. Frequency for Yb is plotted at twice the scale as that for Ce, as the concentration range of an element decreases as incompatibility decreases. The dot-dashed line represents the composition of clinopyroxene in the model DM source (Workman and Hart, 2005). The gray dashed lines show increments of 2% melting (up to 8% for Ce and 18% for Yb) for the nonmodal fractional melting reference model discussed in the text.

term encompasses the processes experienced by abyssal peridotites containing dunite, gabbro or pyroxenite veins, as well as the "other metasomatized peridotites". This latter group may reflect peridotites that record diffuse, non-channelized melt flow, as samples in this category are often suggested to have undergone fertilization by low volume melts percolating along grain boundaries (Seyler et al., 2001, 2004, 2007; Brunelli et al., 2006; Warren and Shimizu, 2010).

Melt–rock interaction can help to explain the large compositional range of harzburgites, which cannot reflect variations in degree of melting alone. For example, harzburgites cover the full range of spinel Cr# (Fig. 5), despite containing <5% clinopyroxene. Even among the most refractory harzburgites (<1% clinopyroxene), spinel Cr# and clinopyroxene trace elements cover the same range as observed in more fertile peridotites (Fig. 13). Harzburgites also show a similar range in Ce and Yb as veined peridotites in histograms of REE abundances (Fig. 14). Samples with low trace element concentrations may reflect high degrees of melting, pre-existing depletion, or both. Samples with high concentrations may reflect lower degrees of melting, higher degrees of melting followed by refertilization, or melting combined with pre-existing compositional heterogeneity.

In abyssal peridotites, open-system melting models produce a better fit to trace element patterns than fractional melting models (Johnson and Dick, 1992; Hellebrand et al., 2002a; Brunelli et al., 2006, 2014; Godard et al., 2008; Liang and Peng, 2010). Open system melting models – also referred to as dynamic, continuous, or critical melting – are characterized by a critical porosity, which represents the portion of melt that is retained in the residue during melting, resulting in less depletion among the most incompatible elements than predicted by a fractional melting model (e.g., Maaløe, 1982; McKenzie, 1985; Iwamori, 1993; Ozawa and Shimizu, 1995; Spiegelman, 1996; Vernières et al., 1997; Zou, 1998). The larger range in Ce concentrations relative to Yb among residual peridotites (Fig. 14A–B) can be explained by the influence of open-system melting processes. In addition to critical porosity, other variables that determine the effects of melt addition include melt composition, peridotite composition, melt addition rate, temperature, and pressure. Hence, melt addition does not necessarily re-enrich the host peridotite, as some veined peridotites can have low trace element concentrations (Fig. 14C–F), possibly by formation of late-stage melts from previously melted material. EPR peridotites provide the best demonstration of this, as they often host gabbro veins, but still have overall low trace element abundances and infertile compositions (Constantin et al., 1995; Dick and Natland, 1996).

The occurrence of melt–peridotite interaction is important for understanding the long-term compositional evolution of the Earth. The compositional range of abyssal peridotites – both among veined and unveined samples – indicates that the lithospheric mantle in oceanic plates is variable in composition and more fertile (i.e., higher pyroxene abundances and higher abundances of incompatible elements), on average, than surveys of residual peridotites alone would imply. Veined peridotites are found across the entire spectrum of spreading rates and at most localities where abyssal peridotites have been collected (Fig. 1). At fast spreading rates, veined samples are often relatively infertile (e.g., EPR samples in Table S2) and thus have a limited effect on average lithospheric mantle composition. The effect of trapped melts on lithosphere composition becomes increasingly pronounced as spreading rate decreases. At spreading rates <40 mm/yr, on-axis conductive cooling limits melting and causes increasing amounts of melt to freeze in the mantle (e.g., Bown and White, 1994; Cannat, 1996; Dick et al., 2003; Sleep and Warren, 2014). The occurrence of a crust–mantle mix at low spreading rates has been observed in seismic studies, which have found both reduced crustal thicknesses and velocities intermediate between mantle and gabbroic rocks (Jokat et al., 2003; Lizarralde et al., 2004; Conley and Dunn, 2011). Hence, any estimate of the average composition of subducting plates needs to include the variability in plate structure at slow and ultraslow spreading ridges.

5.4. Pre-existing mantle heterogeneities

The mantle is often treated as having a homogeneous composition, with DM (Zindler and Hart, 1986; Salters and Stracke, 2004; Workman and Hart, 2005) providing a useful estimate for average upper mantle composition. However, many geophysical, geochemical, and geodynamical studies have demonstrated that the mantle is compositionally heterogeneous across a range of length-scales. Geodynamic models show that plate tectonics leads to increasing mantle heterogeneity over time due to the recycling of material back into the mantle (e.g., van Keken et al., 2002; Davies, 2009; Stixrude and Lithgow-Bertelloni, 2012). This is confirmed by velocity anomalies in seismic tomography studies, which are generally interpreted as subducted oceanic lithosphere (e.g., Lekic et al., 2012). Among MORBs, compositional variations have been interpreted as reflecting local (<100 km) scale mantle compositional variability and larger (>100 km) scale potential temperature variations (e.g., Klein and Langmuir, 1989; Dalton et al., 2014; Gale et al., 2014).

The compositional range of abyssal peridotites (Fig. 10) confirms that the upper mantle is heterogeneous across a range of length-scales. Peridotites extend to infertile compositions (low modal clinopyroxene, low trace elements, and high spinel Cr#) at all spreading rates (Fig. 10). As the degree of melting is limited at low spreading rates by conductive cooling (e.g., Bown and White, 1994; Sleep and Barth, 1997), the presence of harzburgites at spreading rates <40 mm/yr implies ancient melt removal. Isotopic analyses of abyssal peridotites confirm that the mantle is heterogeneous, as demonstrated, for example, by the large ranges of $^{143}Nd/^{144}Nd$ and $^{187}Os/^{188}Os$ (Fig. 15). This spread in isotopic compositions has been explained by long-term mantle variability due to ancient episodes of melting, melt extraction, and melt entrapment (Cipriani et al., 2004; Liu et al., 2008; Stracke et al., 2011; Warren et al., 2009; Warren and Shirey, 2012; Lassiter et al., 2014).

Overall, a consensus exists that the mantle is heterogeneous, but the nature of these heterogeneities remains the subject of debate (e.g., Rubin et al., 2009; Lambart et al., 2013; Byerly and Lassiter, 2014). Peridotites provide unique constraints on the nature of mantle heterogeneity, including (1) the existence of ultra-refractory domains; (2) the degree to which heterogeneities are veins versus less lithologically distinct compositional variations; and (3) the lower length-scale limit of heterogeneities. Additionally, the heterogeneity observed globally among abyssal peridotites provides a record of the compositional range of the oceanic lithospheric mantle that will eventually be recycled back into the mantle by subduction.

5.4.1. Evidence for pyroxenite veins

Mantle heterogeneities are frequently assumed to occur as pyroxenite veins – derived from recycled oceanic crust – enclosed in a peridotitic mantle (e.g., Zindler et al., 1984; Allègre and Turcotte, 1986; Hirschmann and Stolper, 1996). In this context, the term "pyroxenite" has been used to refer to any ultramafic lithology that does not plot in the lherzolite/harzburgite/dunite field of the ultramafic ternary (Fig. 3), as well as to pyroxene-rich lithologies that contain garnet. Studies of abyssal peridotites and MORBs have argued for and against the importance of pyroxenites in the generation of oceanic crust (for a review, see Lambart et al., 2013). For example, Hirschmann and Stolper (1996) argued for 3–6% garnet pyroxenite in the mantle based on MORB trace element and isotope systematics, but Pertermann and Hirschmann (2003) subsequently suggested <2% based on experiments on a basaltic pyroxenite. Despite these low abundance estimates, even small amounts of pyroxenite will make a large contribution to oceanic crust due to their lower solidus temperature and higher melt productivity compared to peridotite (Hirschmann and Stolper, 1996; Pertermann and Hirschmann, 2003; Lambart et al., 2012).

In the abyssal peridotite literature, the pyroxenite debate has frequently been framed in the context of whether basalts and

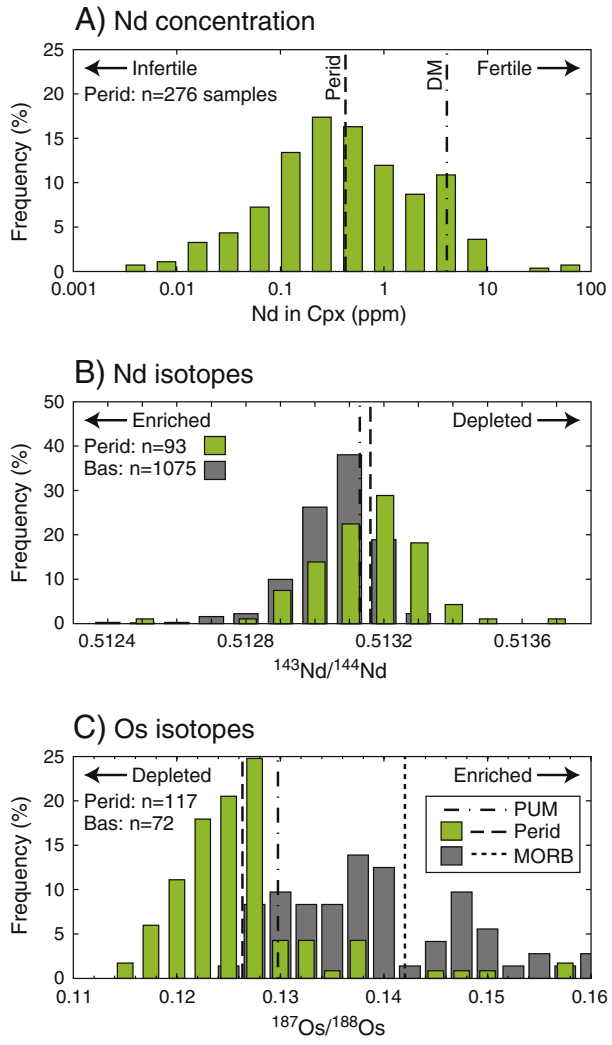

Fig. 15. (A) Histogram of Nd concentrations in clinopyroxene for veined and unveined abyssal peridotites (Tables S1 and S2). The average concentration of Nd in clinopyroxene is 0.4 ppm, while DM clinopyroxene has 4 ppm Nd (Workman and Hart, 2005). (B) Histograms of Nd isotope ratios for clinopyroxene and orthopyroxene from abyssal peridotites (average $^{143}Nd/^{144}Nd = 0.51316$) and global MORB (0.51313). The average value of MORB defines the Nd isotope ratio of DM (Workman and Hart, 2005). Data for peridotite are from the compilation by Warren et al. (2009), with additional data from Mallick et al. (2014). Data for global MORBs are a compilation from PetDB (http://www.petdb.org; Lehnert et al., 2000). (C) Histogram of Os isotope data for bulk rock abyssal peridotites (average $^{187}Os/^{188}Os = 0.142$) compared to global MORBs (0.126) and primitive upper mantle (PUM = 0.129; Meisel et al., 2001). Data for peridotites are from Snow and Reisberg (1995), Brandon et al. (2000), Standish et al. (2002), Alard et al. (2005), Becker et al. (2006), Harvey et al. (2006), Liu et al. (2008), Sichel et al. (2008), and Lassiter et al. (2014). Data for MORBs are from Escrig et al. (2004, 2005) and Gannoun et al. (2007).

peridotites are co-genetic, or whether a component (i.e., pyroxenite) is missing from the dredge record. Comparison of MORB and peridotite isotopic compositions has been used to test whether an offset exists (Snow et al., 1994; Salters and Dick, 2002; Cipriani et al., 2004; Alard et al., 2005; Warren et al., 2009; Mallick et al., 2015). In Fig. 15, Nd and Os isotope compositions are compared for global MORB and abyssal peridotites, as these two isotope systems represent the largest available datasets for peridotites. The difference between MORB and abyssal peridotite for $^{143}Nd/^{144}Nd$ is subtle (Fig. 15B), as MORB has an average value of 0.51306, while abyssal peridotite has an average value of 0.51316. The difference is clearer for $^{187}Os/^{188}Os$ (Fig. 15C), as basalts have an average value of 0.142, while peridotites have an average of 0.126. Some studies have argued that the offset between MORB and peridotite is negligible (e.g., Cipriani et al., 2004; Alard et al., 2005; Warren et al., 2009), with the Os offset reflecting seawater contamination combined with problems in how data are filtered to remove this effect (Alard et al., 2005). Offsets in the isotope datasets may also reflect a mass balance issue when individual melts coalesce to form MORB, as isotopically depleted components must also have lower trace element concentrations, hence depleted components will be diluted by more enriched components when melts from different sources mix (e.g., Warren et al., 2009). Abyssal peridotites may also undersample the depleted component if they too have undergone recent refertilization at the ridge. Alternatively, the isotopic offset has been explained by the preferential melting of isotopically enriched pyroxenite veins – or some other isotopically enriched and fertile component – relative to peridotite (e.g., Salters and Dick, 2002; Liu et al., 2008; Byerly and Lassiter, 2014).

Another argument that has been used both for and against the existence of pyroxenites is the absence of primary pyroxenites among lithologies recovered from the seafloor. Garnet pyroxenite is not recovered from ridges as the slow uplift rate of the mantle allows time for the garnet-to-spinel phase transition to occur. Spinel and plagioclase pyroxenites (Fig. 3E and Table S2) have been recovered from ridges, but have been interpreted as the results of recent melt crystallization (Constantin et al., 1995; Constantin, 1999; Tartarotti et al., 2002; Dantas et al., 2007; Warren et al., 2009; Brunelli and Seyler, 2010; Laukert et al., 2014). Hydrothermal alteration and seafloor weathering do not explain the lack of pyroxenites, as pyroxenite can be distinguished from peridotite at high degrees of alteration and has not hindered the identification of secondary pyroxenites from all ridges (Table 1). The absence of primary pyroxenites has lead to the argument that this component melts out beneath ridges, with some models suggesting that peridotites do not contribute significantly to melt generation (e.g., Salters and Dick, 2002; Stixrude and Lithgow-Bertelloni, 2012; Mallick et al., 2015). However, thermodynamic constraints on pyroxenite melting indicate that they do not undergo 100% melting, though they will undergo a much higher degree of melting than peridotite (Hirschmann and Stolper, 1996; Lambart et al., 2013). While Pertermann and Hirschmann (2003) estimated pyroxenite melting of ~70–90% based on their experiments, more recent calculations based on a range of pyroxenite compositions indicate <40% melting (Lambart et al., 2009; Shorttle et al., 2014). In addition, if pyroxenite melting entirely suppresses peridotite melting, then the compositional variability observed among abyssal peridotites would have to be an entirely inherited signature.

The solution to the question of the relationship between MORB, peridotite, and pyroxenite probably lies in the 5% of secondary pyroxenites that have been recovered from the seafloor. Some of these pyroxenites may correspond to primary pyroxenites that have been modified by recent melting and melt–rock interaction. As discussed by Lambart et al. (2013), primary pyroxenites in the mantle should range from silica-enriched (if derived from MORB) to silica-depleted (if derived from lower oceanic crust such as troctolite or olivine-gabbro), in addition to any pyroxenites previously formed at ridges that were subsequently recycled back into the mantle. A range of reactions can occur between pyroxenites – particularly when they are silica-depleted – and peridotites, both subsolidus and once melts form, which could explain the range of secondary pyroxenites compositions recovered from the seafloor (Sobolov et al., 2007; Herzberg, 2011; Lambart et al., 2013). This model is supported by the observation of Warren et al. (2009) that pyroxenite veins and host peridotites from a single SWIR dredge do not have a clear isotopic or trace element distinction between the two lithologies. If the pyroxenites were primary, they should be isotopically and trace element enriched compared to the peridotite. Instead, both lithologies have similar trace element compositions and span an isotopic range from enriched to depleted, which fits better with a process involving interaction between pyroxenite melt and peridotite. Hence, abyssal peridotites and MORBs are probably not entirely co-genetic, with abyssal pyroxenites corresponding to another

source component for MORB, if they represent modified primary pyroxenites.

The 5% abundance of abyssal pyroxenites agrees remarkably well with the 2–5% abundance of pyroxenite veins in orogenic peridotites and xenoliths (Hirschmann and Stolper, 1996). These abundances correspond to the lithosphere after melting, not the abundance prior to melting, which is a much more difficult estimate to make. For example, Shorttle et al. (2014) estimated that the mantle beneath Iceland contains 4–10% pyroxenite, but a unique solution can only be derived if mantle potential temperature is known exactly. In addition, Shorttle et al. (2014) modeled the mantle as three components, consisting of lherzolite, pyroxenite and harzburgite. Based on evidence for ultra-refractory domains in the mantle, the presence of fertile and infertile peridotite components, along with pyroxenites, probably represents a better model for mantle source composition compared to the peridotite–pyroxenite model.

5.4.2. Ultra-refractory mantle domains

Major, trace, and isotopic datasets for peridotites indicate that sections of the mid-ocean ridge system are underlain by refractory harzburgites that undergo limited melting at the present-day ridge axis. The 15–16°N region around the Fifteen-Twenty transform fault on the MAR represents the best-studied example of an ultra-refractory mantle block, based on infertile major, trace, and modal compositions (Paulick et al., 2006; Kelemen et al., 2007; Seyler et al., 2007; Godard et al., 2008) and unradiogenic Os isotopic compositions (Harvey et al., 2006). Other ridge localities that have harzburgite as the dominant lithology include the easternmost SWIR (Seyler et al., 2004), Lena Tough (Lassiter et al., 2014), and portions of the Sparsely Magmatic Zone on the Gakkel (D'Errico et al., 2016). All these localities have limited amounts of basaltic crust, whereas the high degree of melting required to generate harzburgites should produce ~6 km thick crust, as observed at the EPR. Conversely, some peridotites – such as those from the Romanche transform fault on the MAR (Seyler and Bonatti, 1997) – extend to more fertile compositions than DM, implying enriched source mantle in some regions.

In addition to major and trace element observations of infertile compositions, some abyssal peridotites have isotopic compositions that are more depleted than MORB (Fig. 15). This observation has been made at all three ridges (SWIR, MAR, and Gakkel) where peridotites have been analyzed for isotopes and for all the long-lived radiogenic isotope systems: Nd (Cipriani et al., 2004; Salters and Dick, 2002; Mallick et al., 2014), Sr (Warren et al., 2009), Pb (Warren and Shirey, 2012), Hf (Stracke et al., 2011; Mallick et al., 2015) and Os (Harvey et al., 2006). Ultra-depleted isotopic compositions provide unequivocal evidence for pre-existing depletions, as they require previous episodes of melt extraction to allow time for in-growth of depleted ratios. Peridotites from the harzburgitic sections of the MAR Fifteen-Twenty, Gakkel SMZ, and Lena Trough all extend to unradiogenic $^{187}Os/^{188}Os$, corresponding to rhenium depletion ages up to ~2 Ga (Harvey et al., 2006; Liu et al., 2008; Lassiter et al., 2014). Ocean island xenoliths also provide evidence for ancient, melt-depleted components in the mantle, based on highly depleted isotopic compositions (e.g., Bizimis et al., 2007) and infertile major and trace element compositions (Simon et al., 2008).

The presence and composition of ultra-refractory mantle domains can be difficult to determine from basalt compositions as ultra-refractory material undergoes little or no melting. For example, modeling calculations by Byerly and Lassiter (2014) suggest that infertile mantle with <1 wt.% Al_2O_3 will not generate a significant volume of melt. At the Fifteen-Twenty transform fault, >90% of peridotites have <1 wt.% Al_2O_3 (Paulick et al., 2006; Godard et al., 2008). Thus, refractory peridotites in regions such as this, which also have thin or absent crust, probably represent an ancient, melt-depleted mantle component that has undergone little recent melting. Globally, ~10% of abyssal peridotites from slow and ultraslow ridges contain <1 wt.% bulk Al_2O_3. Combined with isotopic data, this suggests the occurrence of a globally distributed infertile component in the mantle that does not contribute significantly to the generation of oceanic crust. Shorttle et al. (2014) estimated that ~20% of the mantle beneath Iceland consists of a refractory component based on combining crustal thickness constraints with basalt geochemistry. Lassiter et al. (2014) used global peridotite bulk rock Al_2O_3 and $^{187}Os/^{188}Os$ compositions to suggest that the mantle is less fertile than implied by current DM estimates.

Ultra-refractory peridotites probably form in most tectonic settings, including ridges, subduction zones and plumes. For example, bulk rock EPR peridotites have an average of 0.8 ± 0.2 wt.% Al_2O_3 based on 28 samples (Blum, 1991; Party, 1993; Constantin, 1995; Niu and Hékinian, 1997a), indicating that ultra-refractory peridotites form at ridges when the spreading rate is fast enough that melting is not limited by conductive cooling. Peridotites with unradiogenic Os have sometimes been taken as evidence for the presence of subcontinental lithospheric mantle recycled into the convecting upper mantle. However, this interpretation is non-unique, as unradiogenic Os can form in any piece of mantle that has undergone Re removal due to ancient melt depletion (Brandon et al., 2000; Harvey et al., 2006; Warren and Shirey, 2012; Lassiter et al., 2014).

Refractory peridotites may not always have depleted isotopic compositions. On average, a peridotite with low modal clinopyroxene (e.g., infertile) has lower Yb and higher spinel Cr# than peridotite with abundant clinopyroxene (e.g., fertile) (Fig. 13). However, at low clinopyroxene abundance, the trace element abundances in harzburgites are highly variable. For example, peridotites with <2% clinopyroxene have Nd concentrations of 0.01–2 ppm, compared to the range for all residual peridotites of 0.01–5 ppm (Fig. 15A). Peridotites with low modal clinopyroxene are expected to have low trace element concentrations and thus evolve to depleted isotopic compositions. However, the high trace element abundance in a subset of refractory harzburgites (Fig. 13C) indicates that infertile mantle can also evolve to relatively enriched isotopic ratios.

6. Conclusions

Abyssal peridotites are exposed on the seafloor at transform faults and ridges where uplift by faulting exposes lower crustal and upper mantle sections of the oceanic lithosphere. Globally, abyssal peridotites span a large compositional range and extend to infertile compositions at all spreading rates. These two observations indicate that, in addition to recording melt depletion, abyssal peridotite compositions reflect melt–rock interaction and pre-existing compositional heterogeneities. The DM source model provides a useful starting point for exploring mantle melting, but will result in an over- or under-estimation of degree of melting depending on the true initial composition.

Melting and melt extraction in the oceanic upper mantle are often assumed to be two distinct processes, such that melt and mantle do not significantly interact following melt formation. Yet the occurrence of melt–rock interaction is readily observed in veined samples, which form 28% of the global sample set and occur at 73% of sites where residual peridotites are found. In residual peridotites, distinguishing between melt–rock reaction, degree of melting and initial heterogeneity requires careful analysis. Trace element modeling using fractional melting alone is not able to reproduce the abundances of LREE and other highly incompatible elements, whereas models that incorporate a component of open-system melting can reproduce abundances. This implies that melt–rock interaction is a pervasive process at ridges and that all abyssal peridotite are affected to some degree by melt transport. The consequence of this interaction is a heterogeneous oceanic lithosphere, which is eventually recycled back into the mantle, producing further heterogeneity. In addition, the average composition of the oceanic lithospheric mantle is not as depleted as residual peridotites alone would imply.

The major, trace, modal, and isotopic composition of abyssal peridotites provides some key constraints on the nature of mantle heterogeneities. The creation of lithological and chemical variations in peridotites by the ridge melting process suggests that the mantle can be heterogeneous down to very small length-scales, limited only by the subsequent time available for diffusive equilibration. Pyroxenite veins in abyssal samples are not primary recycled oceanic crust, but some may be melts of primary pyroxenites that subsequently reacted with peridotite. Based on the occurrence of refractory harzburgites at most ridges, including regions with limited basaltic crust, refractory domains appear to be scattered throughout the mantle. Overall, the mantle probably contains at least three components (lherzolite, harzburgite, and pyroxenite). As the abyssal peridotite dataset continues to grow, more enriched and depleted mantle domains will be identified and a more nuanced picture of mantle compositional variations will emerge.

Acknowledgments

This work originates from discussions over the years with Peter Kelemen, Nobu Shimizu, Henry Dick, Greg Hirth, Glenn Gaetani, and Fred Frey. More recent discussions with Rich Katz, Bob Coleman, Suzanne Birner, Megan D'Errico, Nik Deems, and Katie Kumamoto have helped to clarify the ideas presented here. Comments from the editor Andrew Kerr and reviewers Shoji Arai and Michael Bizimis helped to improved this article. I am grateful to Andrew Kerr and Tim Horscroft for the invitation to write this review and for their patience throughout the process. Yan Liang and Chenguang Sun provided feedback on their models and the olivine/melt and orthopyroxene/melt partition coefficients included in Table S3. All data used to generate figures are given in the tables and the fractional melting model is provided as a Matlab script in the supplemental material. The research leading to these results has received funding from the US National Science Foundation under NSF grants EAR-1255620 and OCE-1434199 and from the European Research Council under the European Union's Seventh Framework Programme (FP7/2007–2013)/ERC grant agreement number 279925.

Appendix A. Supplementary data

Supplementary data associated with this article can be found in the online version, at http://dx.doi.org/10.1016/j.lithos.2015.12.023. These data include the Google map of the 282 sites (Table 1) described in this article.

References

Abelson, M., Agnon, A., 1997. Mechanics of oblique spreading and ridge segmentation. Earth and Planetary Science Letters 148, 405–421.
Achenbach, K.L., 2008. Melt and Deformation in the Mantle Beneath Mid-ocean Ridges: A Textural and Lattice-preferred Orientation Study of Abyssal Peridotites Ph.D. thesis, University of Wyoming (December).
Aharonov, E., Whitehead, J.A., Kelemen, P.B., Spiegelman, M., 1995. Channeling instability of upwelling melt in the mantle. Journal of Geophysical Research 100 (B10), 20433–20450.
Alard, O., Luguet, A., Pearson, N.J., Griffin, W.L., Lorand, J.-P., Gannoun, A., Burton, K.W., O'Reilly, S.Y., 2005. *In situ* Os isotopes in abyssal peridotites bridge the isotopic gap between MORBs and their source mantle. Nature 436, 1005–1008.
Allègre, C.J., Turcotte, D.L., 1986. Implications of a two-component marble-cake mantle. Nature 323, 123–127.
Anders, E., Grevesse, N., 1989. Abundances of the elements: meteoritic and solar. Geochimica et Cosmochimica Acta 53, 197–214.
Arai, S., 1987. An estimation of the least depleted spinel peridotite on the basis of olivine–spinel mantle array. Neues Jahrbuch Fur Mineralogie — Monatshefte 8, 347–354.
Arai, S., 1992. Chemistry of chromian spinel in volcanic rocks as a potential guide to magma chemistry. Mineralogical Magazine 56, 173–184.
Arai, S., Ishimaru, S., 2008. Insights into petrological characteristics of the lithosphere of mantle wedge beneath arcs through peridotite xenoliths: a review. Journal of Petrology 49 (4), 665–695.
Arai, S., Matsukage, K., 1996. Petrology of the gabbro–troctolite–peridotite complex from Hess Deep, equatorial Pacific: implications for mantle–melt interaction within the oceanic lithosphere. In: Mével, C., Gillis, K.M., Allan, J.F., Meyer, P.S. (Eds.), Proceedings of the Ocean Drilling Program, Scientific Results Vol. 147. College Station, TX, pp. 135–155.
Argus, D.F., Gordon, R.G., 1991. No-net-rotation model of current plate velocities incorporating plate motion model NUVEL-1. Geophysical Research Letters 18 (11), 2039–2042.
Asimow, P.D., 1999. A model that reconciles major- and trace-element data from abyssal peridotites. Earth and Planetary Science Letters 169, 303–319.
Asimow, P.D., Hirschmann, M.M., Ghiorso, M.S., O'Hara, M.J., Stolper, E.M., 1995. The effect of pressure-induced solid-solid phase transitions on decompression melting of the mantle. Geochimica et Cosmochimica Acta 59 (21), 4489–4506.
Bach, W., Garrido, C.J., Paulick, H., Harvey, J., Rosner, M., 2004. Seawater–peridotite interactions: first insights from ODP Leg 209, MAR 15°N. Geochemistry, Geophysics, and Geosystems 5 (9).
Batanova, V.G., Suhr, G., Sobolov, A.V., 1998. Origin of geochemical heterogeneity in the mantle peridotites from the Bay of Islands ophiolite, Newfoundland, Canada: ion probe study of clinopyroxenes. Geochimica et Cosmochimica Acta 62 (5), 853–866.
Becker, H., Horan, M.F., Walker, R.J., Gao, S., Lorand, J.-P., Rudnick, R.L., 2006. Highly siderophile element composition of the Earth's primitive upper mantle: constraints from new data on perdotite massifs and xenoliths. Geochimica et Cosmochimica Acta 70, 4528–4550.
Behn, M.D., Grove, T.L., 2015. Melting systematics in mid-ocean ridge basalts: application of a plagioclase–spinel melting model to global variations in major element chemistry and crustal thickness. Journal of Geophysical Research 120, 4863–4886.
Behn, M.D., Boettcher, M.S., Hirth, G., 2007. Thermal structure of oceanic transform faults. Geology 35 (4), 307–310.
Bizimis, M., Griselin, M., Lassiter, J.C., Salters, V.J.M., Sen, G., 2007. Ancient recycled mantle lithosphere in the Hawaiian plume: osmium–hafnium isotopic evidence from peridotite mantle xenoliths. Earth and Planetary Science Letters 257, 259–273.
Blum, N., 1991. Structure and Composition of Oceanic Crust and Upper Mantle Exposed in Hess Deep of the Galapagos Microplate (Equatorial East Pacific) Ph.D. thesis Universität Karlsruhe, Karlsruhe, Germany.
Bodinier, J.-L., Godard, M., 2014. Orogenic, ophiolitic, and abyssal peridotites. In: Carlson, R.W. (Ed.), 2nd Edition Treatise on Geochemistry Vol. 3. Elsevier, pp. 103–167 (Ch. 4).
Bonatti, E., 1968. Ultramafic rocks from the Mid-Atlantic Ridge. Nature 219 (5152), 363–364.
Bonatti, E., Peyve, A., Kepezhinskas, P., Kurentsova, N., Seyler, M., Skolotnev, S., Udintsev, G., 1992. Upper mantle heterogeneity below the Mid-Atlantic Ridge, 0°–15°N. Journal of Geophysical Research 97 (B4), 4461–4476.
Bonatti, E., Seyler, M., Sushevskaya, N., 1993. A cold suboceanic mantle belt at the Earth's equator. Science 261, 315–320.
Borghini, G., Fumagalli, P., Rampone, E., 2010. The stability of plagioclase in the upper mantle: subsolidus experiments on fertile and depleted lherzolite. Journal of Petrology 51 (1–2), 229–254.
Boschi, C., Früh-Green, G.L., Delacour, A., Karson, J.A., Kelley, D.S., 2006. Mass transfer and fluid flow during detachment faulting and development of an oceanic core complex, Atlantis Massif (MAR 30°N). Geochemistry, Geophysics, and Geosystems 7 (1).
Bown, J.W., White, R.S., 1994. Variation with spreading rate of oceanic crustal thickness and geochemistry. Earth and Planetary Science Letters 121, 435–449.
Brandon, A.D., Snow, J.E., Walker, R.J., Morgan, J.W., Mock, T.D., 2000. ^{190}Pt–^{186}Os and ^{187}Re–^{187}Os systematics of abyssal peridotites. Earth and Planetary Science Letters 177, 319–335.
Brunelli, D., Seyler, M., 2010. Asthenospheric percolation of alkaline melts beneath the St. Paul region (Central Atlantic Ocean). Earth and Planetary Science Letters 289 (3–4), 393–405.
Brunelli, D., Cipriani, A., Ottolini, L., Peyve, A.A., Bonatti, E., 2003. Mantle peridotites from the Bouvet Triple Junction Region, South Atlantic. Terra Nova 15 (3), 194–203.
Brunelli, D., Seyler, M., Cipriani, A., Ottolini, L., Bonatti, E., 2006. Discontinuous melt extraction and weak refertilization of mantle peridotites at the Vema Lithospheric Section (Mid-Atlantic Ridge). Journal of Petrology 47 (4), 745–771.
Brunelli, D., Paganelli, E., Seyler, M., 2014. Percolation of enriched melts during incremental open-system melting in the spinel field: a REE approach to abyssal peridotites from the Southwest Indian Ridge. Geochimica et Cosmochimica Acta 127, 190–203.
Bryndzia, L.T., Wood, B.J., 1990. Oxygen thermobarometry of abyssal spinel peridotites; the redox state and C–O–H volatile composition of the Earth's sub-oceanic upper mantle. American Journal of Science 290 (10), 1093–1116.
Bryndzia, L.T., Wood, B.J., Dick, H.J.B., 1989. The oxidation state of the earth's sub-oceanic mantle from oxygen thermobarometry of abyssal spinel peridotites. Nature 341, 526–527.
Byerly, B.L., Lassiter, J.C., 2014. Isotopically ultradepleted domains in the convecting upper mantle: implications for MORB petrogenesis. Geology 42 (3), 203–206.
Cann, J.R., Blackman, D.K., Smith, D.K., McAllister, E., Janssen, B., Mello, S., Avgerinos, E., Pascoe, A.R., Escartin, J., 1997. Corrugated slip surfaces formed at ridge-transform intersections on the Mid-Atlantic Ridge. Nature 385, 329–332.
Cannat, M., 1996. How thick is the magmatic crust at slow spreading ridges. Journal of Geophysical Research 101 (B2), 2847–2857.
Cannat, M., Seyler, M., 1995. Transform tectonics, metamorphic plagioclase and amphibolitization in ultramafic rocks of the Vema transform fault (Atlantic Ocean). Earth and Planetary Science Letters 133, 283–298.
Cannat, M., Bideau, D., Hébert, R., 1990. Plastic deformation and magmatic impregnation in serpentinized ultramafic rocks from the Garrett transform fault (East Pacific Rise). Earth and Planetary Science Letters 101 (216–232).
Cannat, M., Bideau, D., Bougault, H., 1992. Serpentinized peridotites and gabbros in the Mid-Atlantic Ridge axial valley at 15°37′N and 16°52′N. Earth and Planetary Science Letters 109, 87–106.

Chalot-Prat, F., Falloon, T.J., Green, D.H., Hibberson, W.O., 2013. Melting of plagioclase + spinel lherzolite at low pressures (0.5 GPa): an experimental approach to the evolution of basaltic melt during mantle refertilisation at shallow depths. Lithos 172–173, 61–80.
Cipriani, A., Brueckner, H.K., Bonatti, E., Brunelli, D., 2004. Oceanic crust generated by elusive parents: Sr and Nd isotopes in basalt–peridotite pairs from the Mid-Atlantic Ridge and Nd isotopes in basalt–peridotite pairs from the Mid-Atlantic Ridge. Geology 32 (8), 657–660.
Cipriani, A., Bonatti, E., Seyler, M., Brueckner, H.K., Brunelli, D., Dallai, L., Hemming, S.R., Ligi, M., Ottolini, L., Turrin, B.D., 2009 bb. A 19 to 17 Ma amagmatic extension event at the Mid-Atlantic Ridge: ultramafic mylonites from the Vema Lithospheric Section. Geochemistry, Geophysics, and Geosystems 10, Q10011.
Cipriani, A., Bonatti, E., Brunelli, D., Ligi, M., 2009a. 26 million years of mantle upwelling below a segment of the Mid Atlantic Ridge: the Vema Lithospheric Section revisited. Earth and Planetary Science Letters 285, 87–95.
Conley, M.M., Dunn, R.A., 2011. Seismic shear wave structure of the uppermost mantle beneath the Mohns Ridge. Geochemistry, Geophysics, and Geosystems 12 (10), Q0AK01.
Constantin, M., 1995. Pétrologie des gabbros et péridotites de la dorsale Est-Pacifique: la transition croute-manteau aux dorsales rapides Ph.D. thesis Université de Bretagne Occidentale, Brest, France.
Constantin, M., 1999. Gabbroic intrusions and magmatic metasomatism in harzburgites from the Garrett transform fault: implications for the nature of the mantle–crust transition at fast-spreading ridges. Contributions to Mineralogy and Petrology 136, 111–130.
Constantin, M., Hékinian, R., Ackermand, D., Stoffers, P., 1995. Mafic and ultramafic intrusions into upper mantle peridotites from fast spreading centers of the Easter Microplate (South East Pacific). In: Vissers, R.L.M., Nicolas, A. (Eds.), Mantle and Lower Crust Exposed in Oceanic Ridges and in Ophiolites. Kluwer Academic Publishers, pp. 71–120.
Coogan, L.A., Thompson, G.M., MacLeod, C.J., Dick, H.J.B., Edwards, S.J., Hosford Scheirer, A., Barry, T.L., 2004. A combined basalt and peridotite perspective on 14 million years of melt generation at the Atlantis Bank segment of the Southwest Indian Ridge: evidence for temporal changes in mantle dynamics. Chemical Geology 207, 13–30.
D'Errico, M.E., Warren, J.M., Godard, M., 2016. Evidence for chemically heterogeneous Arctic mantle beneath the Gakkel Ridge. Geochimica et Cosmochimica Acta 174, 291–312. http://dx.doi.org/10.1016/j.gca.2015.11.017.
Daines, M.J., Kohlstedt, D.L., 1994. The transition from porous to channelized flow due to melt/rock reaction during melt migration. Geophysical Research Letters 21 (2), 145–148.
Dalton, C.A., Langmuir, C.H., Gale, A., 2014. Geophysical and geochemical evidence for deep temperature variations beneath mid-ocean ridges. Science 344, 80–83.
Dantas, C., Ceuleneer, G., Gregoire, M., Python, M., Freydier, R., Warren, J.M., Dick, H.J.B., 2007. Pyroxenites from the Southwest Indian Ridge, 9–16°E: cumulates from incremental melt fractions produced at the top of a cold melting regime. Journal of Petrology 48 (4), 647–660.
Davies, G.F., 2009. Reconciling the geophysical and geochemical mantles: plume flows, heterogeneities, and disequilibrium. Geochemistry, Geophysics, and Geosystems 10 (10), Q10008 (October).
Dick, H.J.B., 1989. Abyssal peridotites, very slow spreading ridges and ocean ridge magmatism. In: Saunders, A.D., Norry, M.J. (Eds.), Magmatism in the Ocean Basins. No. 42 in Special Publication. Geological Society of London, pp. 71–105.
Dick, H.J.B., Bullen, T., 1984. Chromian spinel as a petrogenetic indicator in abyssal and alpine-type peridotites and spatially associated lavas. Contributions to Mineralogy and Petrology 86, 54–76.
Dick, H.J.B., Natland, J.H., 1996. Late-stage melt evolution and transport in the shallow mantle beneath the East Pacific Rise. In: Mével, C., Gillis, K.M., Allan, J.F., Meyer, P.S. (Eds.), Proceedings of the Ocean Drilling Program, Scientific Results Vol. 147. College Station, TX, pp. 103–134.
Dick, H.J.B., Fisher, R.L., Bryan, W.B., 1984. Mineralogic variability of the uppermost mantle along mid-ocean ridges. Earth and Planetary Science Letters 69, 88–106.
Dick, H.J.B., Lin, J., Schouten, H., 2003. An ultraslow-spreading class of ocean ridge. Nature 426, 405–412.
Dick, H.J.B., Tivey, M.A., Tucholke, B.E., 2008. Plutonic foundation of a slow-spreading ridge segment: oceanic core complex at Kane Megamullion, 23°30′N, 45°20′W. Geochemistry, Geophysics, and Geosystems 9 (5).
Dick, H.J.B., Lissenberg, C.J., Warren, J.M., 2010. Mantle melting, melt transport and delivery beneath a slow-spreading ridge: the paleo-MAR from 23°15′N to 23°45′N. Journal of Petrology 51 (1–2), 425–467.
Dijkstra, A.H., Drury, M.R., Vissers, R.L.M., 2001. Structural petrology of plagioclase peridotites in the west Othris Mountains (Greece): melt impregnation in mantle lithosphere. Journal of Petrology 42, 5–24.
Dosso, L., Bougault, H., Langmuir, C., Bollinger, C., Bonnier, O., Etoubleau, J., 1999. The age and distribution of mantle heterogeneity along the Mid-Atlantic Ridge (31–41°N). Earth and Planetary Science Letters 170, 269–286.
Droop, G.T.R., 1987. A general equation for estimating Fe^{3+} concentrations in ferromagnesian silicates and oxides from microprobe analyses, using stoichimetric criteria. Mineralogical Magazine 51, 431–435.
Dupré, B., Allègre, C.J., 1983. Pb–Sr isotope variation in Indian Ocean basalts and mixing phenomena. Nature 303, 142–146.
Elliott, T., Spiegelman, M., 2003. Melt migration in oceanic crustal production: a U-series perspective. In: Rudnick, R.L. (Ed.), Treatise on Geochemistry Vol. 3. Elsevier, pp. 465–510.
Engel, C.G., Fisher, R.L., 1969. Lherzolite, anorthosite, gabbro, and basalt dredged from the Mid-Indian Ocean Ridge. Science 166, 1136–1141.
Escrig, S., Capmas, F., Dupré, B., Allègre, C.J., 2004. Osmium isotopic constraints on the nature of the DUPAL anomaly from Indian mic-ocean-ridge basalts. Nature 431, 59–63.
Escrig, S., Schiano, P., Schilling, J.-G., Allègre, C.J., 2005. Rhenium–osmium isotope systematics in MORB from the Southern Mid-Atlantic Ridge (40°–50°S). Earth and Planetary Science Letters 235, 528–548.
Falloon, T.J., Green, D.H., Danyushevsky, L.V., McNeill, A.W., 2008. The composition of near-solidus partial melts of fertile peridotite at 1 and 1.5 GPa: implications for the petrogenesis of MORB. Journal of Petrology 49 (4), 591–613.
Floyd, J.S., Tolstoy, M., Mutter, J.C., Scholz, C.H., 2002. Seismotectonics of mid-ocean ridge propagation in Hess Deep. Science 298, 1765–1768.
Forsyth, D.W., 1993. Crustal thickness and the average depth and degree of melting in fractional melting models of passive flow beneath mid-ocean ridges. Journal of Geophysical Research 98 (B9), 16073–16079.
Fujii, T., 1990. Petrology of peridotites from Hole 670A, Leg 109. In: Detrick, R., Honnorez, J., Bryan, W.B., Juteau, T., et al. (Eds.), Proceedings of the Ocean Drilling ProgramScientific Results. Vol. 106/109. College Station, TX, pp. 19–25.
Gale, A., Dalton, C.A., Langmuir, C.H., Su, Y., Schilling, J.-G., 2013. The mean composition of ocean ridge basalts. Geochemistry, Geophysics, and Geosystems 14 (3).
Gale, A., Langmuir, C.H., Dalton, C.A., 2014. The global systematics of ocean ridge basalts and their origin. Journal of Petrology 55 (6), 1051–1082.
Gannoun, A., Burton, K.W., Parkinson, I.J., Alard, O., Schiano, P., Thomas, L.E., 2007. The scale and origin of the osmium isotope variations in mid-ocean ridge basalts. Earth and Planetary Science Letters 259, 541–556.
Gasparik, T., 1987. Orthopyroxene thermobarometry in simple and complex systems. Contributions to Mineralogy and Petrology 96 (3), 357–370.
Gast, P.W., 1968. Trace element fractionation and the origin of tholeiitic and alkaline magma types. Geochimica et Cosmochimica Acta 32, 1057–1086.
Ghose, I., Cannat, M., Seyler, M., 1996. Transform fault effect on mantle melting in the MARK area (Mid-Atlantic Ridge south of the Kane transform). Geology 24 (12), 1139–1142.
Godard, M., Lagabrielle, Y., Alard, O., Harvey, J., 2008. Geochemistry of the highly depleted peridotites drilled at ODP Sites 1272 and 1274 (Fifteen-Twenty Fracture Zone, Mid-Atlantic Ridge): implications for mantle dynamics beneath a slow spreading ridge. Earth and Planetary Science Letters 267, 410–425.
Green, D.H., 1964. The petrogenesis of the high-temperature peridotite intrusion in the Lizard area, Cornwall. Journal of Petrology 5 (1), 134–188.
Green, D.H., Hibberson, W., 1970. The instability of plagioclase in peridotite at high pressure. Lithos 3 (3), 209–221.
Green, D.H., Ringwood, A.E., 1968. The stability fields of aluminous pyroxene peridotite and garnet peridotite and their relevance in upper mantle structure. Earth and Planetary Science Letters 3, 151–160.
Hamelin, B., Dupré, B., Allègre, C.J., 1985. Pb–Sr–Nd isotopic data of Indian Ocean ridges: new evidence of large-scale mapping of mantle heterogeneities. Earth and Planetary Science Letters 76, 288–298.
Hamlyn, P.R., Bonatti, E., 1980. Petrology of mantle-derived ultramafics from the Owen Fracture Zone, northwest Indian Ocean: implications for the nature of the oceanic upper mantle. Earth and Planetary Science Letters 48, 65–79.
Hart, S.R., Dunn, T., 1993. Experimental cpx/melt partitioning of 24 trace elements. Contributions to Mineralogy and Petrology 113, 1–8.
Hart, S.R., Zindler, A., 1986. In search of a bulk-Earth composition. Chemical Geology 57, 247–267.
Harvey, J., Gannoun, A., Burton, K.W., Rogers, N.W., Alard, O., Parkinson, I.J., 2006. Ancient melt extraction from the oceanic upper mantle revealed by Re–Os isotopes in abyssal peridotites form the Mid-Atlantic ridge. Earth and Planetary Science Letters 244, 606–621.
Harvey, J., Warren, J.M., Shirey, S.B., 2015. Mantle sulfides and their role in Re–Os–Pb geochronology. Reviews in Mineralogy and Geochemistry 81.
Hayman, N.W., Grindlay, N.R., Perfit, M.R., Mann, P., Leroy, S., Mercier de Lépinay, B., 2011. Oceanic core complex development at the ultraslow spreading Mid-Cayman Spreading Center. Geochemistry, Geophysics, and Geosystems 12 (3), Q0AG02.
Hellebrand, E., Snow, J.E., 2003. Deep melting and sodic metasomatism underneath the highly oblique-spreading Lena Trough (Arctic Ocean). Earth and Planetary Science Letters 216, 283–299.
Hellebrand, E., Snow, J.E., Dick, H.J.B., Hofmann, A.W., 2001. Coupled major and trace elements as indicators of the extent of meting in mid-ocean-ridge peridotites. Nature 410, 677–681.
Hellebrand, E., Snow, J.E., Hoppe, P., Hofmann, A.W., December 2002a. Garnet-field melting and late-stage refertilization in 'residual' abyssal peridotites from the Central Indian Ridge. Journal of Petrology 43 (12), 2305–2338.
Hellebrand, E., Snow, J.E., Mühe, R., February 2002b. b. Mantle melting beneath Gakkel Ridge (Arctic Ocean): abyssal peridotite spinel compositions. Chemical Geology 182 (2–4), 227–235.
Hellebrand, E., Snow, J.E., Mostefaoui, S., Hoppe, P., 2005. Trace element distribution between orthopyroxene and clinopyroxene in peridotites from the Gakkel Ridge: a SIMS and NanoSIMS study. Contributions to Mineralogy and Petrology 150, 486–504.
Herzberg, C., 2011. Identification of source lithology in the Hawaiian and Canary Islands: implications for origins. Journal of Petrology 52 (1), 113–146.
Hirschmann, M.M., 2006. Water, melting, and the deep Earth H_2O cycle. Annual Review of Earth and Planetary Sciences 34, 629–653.
Hirschmann, M.M., Stolper, E.M., 1996. A possible role for garnet pyroxenite in the origin of the "garnet signature" in MORB. Contributions to Mineralogy and Petrology 124, 185–208.
Hirschmann, M.M., Tenner, T.J., Aubaud, C., Withers, A.C., 2009. Dehydration melting of nominally anhydrous mantle: the primacy of partitioning. Physics of the Earth and Planetary Interiors 176 (1–2), 54–68.
Iwamori, H., 1993. Dynamic disequilibrium melting model with porous flow and diffusion-controlled chemical equilibration. Earth and Planetary Science Letters 114, 301–313.

Jaroslow, G.E., Hirth, G., Dick, H.J.B., 1996. Abyssal peridotite mylonites: implications for grain-size sensitive flow and strain localization in the oceanic lithosphere. Tectonophysics 256, 17–37.
John, B.E., Cheadle, M.J., 2010. Deformation and alteration associated with oceanic and continental detachment fault systems: are they similar? Geophysical Monograph 188, 175–205.
Johnson, K.T.M., Dick, H.J.B., 1992. Open system melting and temporal and spatial variation of peridotite and basalt at the Atlantis II Fracture Zone. Journal of Geophysical Research 97 (B6), 9219–9241.
Johnson, K.T.M., Dick, H.J.B., Shimizu, N., 1990. Melting in the oceanic upper mantle: an ion microprobe study of diopsides in abyssal peridotites. Journal of Geophysical Research 95, 2661–2678.
Jokat, W., Ritzmann, O., Schmidt-Aursch, M.C., Drachev, S., Gauger, S., Snow, J.E., 2003. Geophysical evidence for reduced melt production on the Arctic ultraslow Gakkel mid-ocean ridge. Nature 423, 962–965.
Juteau, T., Berger, E., Cannat, M., 1990. Serpentinized, residual mantle peridotites from the M.A.R. median valley, ODP Hole 670A (21°10′N, 45°02′W, Leg 109): primary mineralogy and geothermometry. In: Detrick, R., Honnorez, J., Bryan, W.B., Juteau, T., et al. (Eds.), Proceedings of the Ocean Drilling ProgramScientific Results Vol. 106/109. College Station, TX, pp. 27–45.
Katz, R.F., Weatherley, S.M., 2012. Consequences of mantle heterogeneity for melt extraction at mid-ocean ridges. Earth and Planetary Science Letters 335–336, 226–237.
Kelemen, P.B., Dick, H.J.B., Quick, J.E., 1992. Formation of harzburgite by pervasive melt/rock reaction in the upper mantle. Nature 358, 635–641.
Kelemen, P.B., Shimizu, N., Dunn, T., 1993. Relative depletion of niobium in some arc magmas and the continental crust: partitioning of K, Nb, La and Ce during melt/rock reaction in the upper mantle. Earth and Planetary Science Letters 120, 111–134.
Kelemen, P.B., Shimizu, N., Salters, V.J.M., 1995. Extraction of mid-ocean-ridge basalt from the upwelling mantle by focused flow of melt in dunite channels. Nature 375, 747–753.
Kelemen, P.B., Hirth, G., Shimizu, N., Spiegelman, M., Dick, H.J.B., 1997. A review of melt migration processes in the adiabatically upwelling mantle beneath oceanic spreading ridges. Philosophical Transactions of the Royal Society of London A 355, 283–318.
Kelemen, P.B., Yogodzinski, G.M., Scholl, D.W., 2003. Along-strike variation in lavas of the Aleutian island arc: implications for the genesis of high Mg# andesite and the continental crust. In: Eiler, J. (Ed.), The Subduction Factory. Vol. 138 of Geophysical Monograph. American Geophysical Union, pp. 223–276.
Kelemen, P.B., Kikawa, E., Miller, D.J., Party, Shipboard Scientific, 2007. Leg 209 summary: processes in a 20-km-thick conductive boundary layer beneath the Mid-Atlantic Ridge, 14°–16°N. In: Kelemen, P.B., Kikawa, E., Miller, D.J. (Eds.), Proceedings of the Ocean Drilling Program, Scientific ResultsOcean Drilling Program 209. College Station, TX, pp. 1–33.
Kempton, P.D., Stephens, C.J., 1997. Petrology and geochemistry of nodular websterite inclusions in harzburgite, Hole 920D. In: Karson, J.A., Cannat, M., Miller, D.J., Elthon, D. (Eds.), Proceedings of the Ocean Drilling Program, Scientific Results Vol. 153. College Station, TX, pp. 321–331.
Khedr, M.Z., Arai, S., 2010. Hydrous peridotites with Ti-rich chromian spinel as a low-temperature forearc mantle facies: evidence from the Happo-O'ne metaperidotites (Japan). Contributions to Mineralogy and Petrology 159, 137–157.
Kinzler, R.J., 1997. Melting of mantle peridotite at pressures approaching the spinel to garnet transition: application to mid-ocean ridge basalt petrogenesis. Journal of Geophysical Research 102 (B1), 853–874.
Kinzler, R.J., Grove, T.L., 1992. Primary magmas of mid-ocean ridge basalts 1. Experiments and methods. Journal of Geophysical Research 97 (B5), 6885–6906.
Klein, E.M., Langmuir, C.H., 1987. Global correlations of ocean ridge basalt chemistry with axial depth and crustal thickness. Journal of Geophysical Research 92 (B8), 8089–8115.
Klein, E.M., Langmuir, C.H., 1989. Loval versus global variations in ocean ridge basalt composition. Journal of Geophysical Research 94 (B4), 4241–4252.
Klein, F., Bach, W., Jöns, N., McCollom, T., Moskowitz, B., Berquó, T., 2009. Iron partitioning and hydrogen generation during serpentinization of abyssal peridotites from 15°N on the Mid-Atlantic Ridge. Geochimica et Cosmochimica Acta 73, 6868–6893.
Komor, S.C., Grove, T.L., Hébert, R., 1990. Abyssal peridotites from ODP Hole 670A (21°10′N, 45°02′W): residues of mantle melting exposed by non-constructive axial divergence. In: Detrick, R., Honnorez, J., Bryan, W.B., Juteau, T., et al. (Eds.), Proceedings of the Ocean Drilling ProgramScientific Results Vol. 106/109. College Station, TX, pp. 85–101.
Kumagai, H., Dick, H.J.B., Kaneoka, I., 2003. Noble gas signatures of abyssal gabbros and peridotites at an Indian Ocean core complex. Geochemistry, Geophysics, and Geosystems 4 (12). http://dx.doi.org/10.1029/2003GC000540.
Kushiro, I., Yoder, H.S., 1966. Anorthite–forsterite and anorthite–enstatite reactions and their bearing on the basalt–eclogite transformation. Journal of Petrology 7 (3), 337–362.
Lambart, S., Laporte, D., Schiano, P., 2009. An experimental study of pyroxenite partial melts at 1 and 1.5 GPa: implications for the major-element composition of Mid-Ocean Ridge Basalts. Earth and Planetary Science Letters 288, 335–347.
Lambart, S., Laporte, D., Provost, A., Schiano, P., 2012. Fate of pyroxenite-derived melts in the peridotitic mantle: thermodynamic and experimental constraints. Journal of Petrology 53 (3), 451–476.
Lambart, S., Laporte, D., Schiano, P., 2013. Markers of the pyroxenite contribution in the major-element compositions of oceanic basalts: review of the experimental constraints. Lithos 160–161, 14–36.
Lassiter, J.C., Byerly, B.L., Snow, J.E., Hellebrand, E., 2014. Constraints from Os-isotope variations on the origin of Lena Trough abyssal peridotites and implications for the composition and evolution of the depleted upper mantle. Earth and Planetary Science Letters 403, 178–187.
Laukert, G., von der Handt, A., Hellebrand, E., Snow, J.E., Hoppe, P., Klügel, A., 2014. High-pressure reactive melt stagnation recorded in abyssal pyroxenites from the ultraslow-spreading Lena Trough, Arctic Ocean. Journal of Petrology 55 (2), 427–458.
Lehnert, K., Su, Y., Langmuir, C., Sarbas, B., Nohl, U., 2000. A global geochemical database structure for rocks. Geochemistry, Geophysics, and Geosystems 1. http://dx.doi.org/10.1029/1999GC00026.
Lekic, V., Cottaar, S., Dziewonski, A., Romanowicz, B., 2012. Cluster analysis of global lower mantle tomography: a new class of structure and implications for chemical heterogeneity. Earth and Planetary Science Letters 357–358, 68–77.
Liang, Y., Parmentier, E.M., 2010. A two-porosity double lithology model for partial melting, melt transport and melt–rock reaction in the mantle: mass conservation equations and trace element transport. Journal of Petrology 51 (1–2), 125–152.
Liang, Y., Peng, Q., 2010. Non-modal melting in an upwelling mantle column: steady-state models with applications to REE depletion in abyssal peridotites and the dynamics of melt migration in the mantle. Geochimica et Cosmochimica Acta 74, 321–339.
Liang, Y., Schiemenz, A., Hesse, M.A., Parmentier, E.M., Hesthaven, J.S., 2010. Highporosity channels for melt migration in the mantle: top is the dunite and bottom is the harzburgite and lherzolite. Geophysical Research Letters 37, L15306.
Liang, Y., Sun, C., Yao, L., 2013. A REE-in-two-pyroxene thermometer for mafic and ultramafic rocks. Geochimica et Cosmochimica Acta 102, 246–260.
Liu, C.-Z., Snow, J.E., Hellebrand, E., Brügmann, G.E., von der Handt, A.B., Hofmann, A.W., 2008. Ancient, highly heterogeneous mantle beneath Gakkel ridge, Arctic Ocean. Nature 452, 311–316.
Lizarralde, D., Gaherty, J.B., Collins, J.A., Hirth, G., Kim, S.D., 2004. Spreading-rate dependence of melt extraction at mid-ocean ridges from mantle seismic refraction data. Nature 432, 744–747.
Longhi, J.E., 2002. Some phase equilibrium systematics of lherzolite melting: I. Geochemistry, Geophysics, and Geosystems 3 (3).
Lonsdale, P., November 1988. Structural pattern of the Galapagos Microplate and evolution of the Galapagos Triple Junction. Journal of Geophysical Research 93 (B1), 13551–13574.
Loubet, M., Shimizu, N., Allègre, C.J., 1975. Rare earth elements in alpine peridotites. Contributions to Mineralogy and Petrology 53 (1), 1–12.
Luguet, A., Lorand, J.-P., Seyler, M., 2003. Sulfide petrology and highly siderophile element geochemistry of abyssal peridotites: a coupled study of samples from the Kane Fracture Zone (45°W 23°20N, MARK Area, Atlantic Ocean). Geochimica et Cosmochimica Acta 67 (8), 1553–1570.
Maaløe, S., 1982. Geochemical aspects of permeability controlled partial melting and fractional crystallization. Geochimica et Cosmochimica Acta 46, 43–57.
Mallick, S., Dick, H.J.B., Sachi-Kocher, A., Salters, V.J.M., 2014. Isotope and trace element insights into heterogeneity of subridge mantle. Geochemistry, Geophysics, and Geosystems 15, 2438–2453.
Mallick, S., Standish, J.J., Bizimis, M., 2015. Constraints on the mantle mineralogy of an ultra-slow ridge: hafnium isotopes in abyssal peridotites and basalts from the 9–25°E Southwest Indian Ridge. Earth and Planetary Science Letters 410, 42–53.
Malvoisin, B., 2015. Mass transfer in the oceanic lithosphere: serpentinization is not isochemical. Earth and Planetary Science Letters 430, 75–85.
McKenzie, D.P., 1985. ^{230}Th–^{238}U disequilibrium and the melting processes beneath ridge axes. Earth and Planetary Science Letters 72, 149–157.
Meisel, T., Walker, R.J., Irving, A.J., Lorand, J.-P., 2001. Osmium isotopic compositions of mantle xenoliths: a global perspective. Geochimica et Cosmochimica Acta 65 (8), 1311–1323.
Melson, W.G., Jarosewich, E., Bowen, V.T., Thompson, G., 1967. St. Peter and St. Paul rocks: a high-temperature, mantle-derived intrusion. Science 155 (3769), 1532–1535.
Michael, P.J., Bonatti, E., 1985a. Peridotite composition from the North Atlantic: regional and tectonic variations and implications for partial melting. Earth and Planetary Science Letters 73, 91–104.
Michael, P.J., Bonatti, E., 1985b. Petrology of ultramafic rocks from sites 556, 558, and 560 in the north Atlantic. Initial Reports of the Deep Sea Drilling Program 82, 523–528.
Montési, L.G.J., Behn, M.D., 2007. Mantle flow and melting underneath oblique and ultraslow mid-ocean ridges. Geophysical Research Letters 34, L24307.
Morgan, Z., Liang, Y., Kelemen, P.B., 2008. Significance of the concentration gradients associated with dunite bodies in the Josephine and Trinity ophiolites. Geochemistry, Geophysics, and Geosystems 9 (7).
Morishita, T., Maeda, J., Miyashita, S., Kumagai, H., Matsumoto, T., Dick, H.J.B., 2007. Petrology of local concentration of chromian spinel in dunite from the slow-spreading Southwest Indian Ridge. European Journal of Mineralogy 19, 871–882.
Müntener, O., Manatschal, G., Desmurs, L., Pettke, T., 2010. Plagioclase peridotites in ocean–continent transitions: refertilized mantle domains generated by melt stagnation in the shallow mantle lithosphere. Journal of Petrology 51 (1–2), 255–294.
Niida, K., 1997. Mineralogy of MARK peridotites: replacement through magma channeling examined from Hole 920D, MARK Area. In: Karson, J.A., Cannat, M., Miller, D.J., Elthon, D. (Eds.), Proceedings of the Ocean Drilling ProgramScientific Results Vol. 153. College Station, TX, pp. 265–275.
Niida, K., Green, D.H., 1999. Stability and chemical composition of pargasitic amphibole in MORB pyrolite under upper mantle conditions. Contributions to Mineralogy and Petrology 135 (1), 18–40.
Niu, Y., 1997. Mantle melting and melt extraction processes beneath ocean ridges: evidence from abyssal peridotites. Journal of Petrology 38, 1047–1074.
Niu, Y., 2004. Bulk-rock major and trace element compositions of abyssal peridotites: implications for mantle melting, melt extraction and post-melting processes beneath mid-ocean ridges. Journal of Petrology 45 (12), 2423–2458.

Niu, Y., Hékinian, R., 1997a. Basaltic liquids and harzburgitic residues in the Garrett Transform: a case study at fast-spreading ridges. Earth and Planetary Science Letters 146, 243–258.
Niu, Y., Hékinian, R., 1997b. Spreading-rate dependence of the extent of mantle melting beneath ocean ridges. Nature 385, 326–329.
Ozawa, K., Shimizu, N., 1995. Open-system melting in the upper mantle: constraints from the Hayachine–Miyamori ophiolite, northeastern Japan. Journal of Geophysical Research 100 (B11), 22315–22335.
Party, Shipboard Scientific, 1993. Site 895. In: Gillis, K.M., Mével, C., Allan, J.F. (Eds.), Proceedings of the Ocean Drilling Program, Initial ReportsOcean Drilling Program 147. College Station, TX, pp. 109–159.
Paulick, H., Bach, W., Godard, M., De Hoog, J.C.M., Suhr, G., Harvey, J., 2006. Geochemistry of abyssal peridotites (Mid-Atlantic Ridge, 15°20′N, ODP Leg 209): implications for fluid/rock interaction in slow spreading environments. Chemical Geology 234, 179–210.
Pearson, D.G., Canil, D., Shirey, S.B., 2014. Mantle samples included in volcanic rocks: xenoliths and diamonds. In: Carlson, R.W. (Ed.), 2nd Edition Treatise on Geochemistry Vol. 3. Elsevier, pp. 169–253 Ch. 5.
Pertermann, M., Hirschmann, M.M., 2003. Partial melting experiments on a MORB-like pyroxenite between 2 and 3 GPa: constraints on the presence of pyroxenite in basalt source regions from solidus location and melting rate. Journal of Geophysical Research 108 (B2). http://dx.doi.org/10.1029/2000JB000118.
Phipps Morgan, J., Forsyth, D.W., 1988. Three-dimensional flow and temperature perturbations due to a transform offset: effects on oceanic crustal and upper mantle structure. Journal of Geophysical Research 93 (B4), 2955–2966.
Piccardo, G.B., Zanetti, A., Müntener, O., 2007. Melt/peridotite interaction in the Southern Lanzo peridotite: field, textural and geochemical evidence. Lithos 94, 181–209.
Pickering-Witter, J., Johnston, A.D., 2000. The effects of variable bulk composition on the melting systematics of fertile peridotitic assemblages. Contributions to Mineralogy and Petrology 140, 190–211.
Prinz, M., Keil, K., Green, G.A., Reid, A.M., Bonatti, E., Honnorez, J., 1976. Ultramafic and mafic dredge samples from the equatorial mid-Atlantic ridge and fracture zones. Journal of Geophysical Research 81, 4087–4103.
Rampone, E., Hofmann, A.W., 2012. A global overview of isotopic heterogeneities in the oceanic mantle. Lithos 148, 247–261.
Rampone, E., Piccardo, G.B., Vannucci, R., Bottazzi, P., Ottolini, L., 1993. Subsolidus reactions monitored by trace element partitioning: the spinel- to plagioclase-facies transition in mantle peridotites. Contributions to Mineralogy and Petrology 115, 1–17.
Robinson, J.A.C., Wood, B.J., Blundy, J.D., 1998. The beginning of melting of fertile and depleted peridotite at 1.5 GPa. Earth and Planetary Science Letters 155, 97–111.
Roland, E., Behn, M.D., Hirth, G., 2010. Thermal–mechanical behavior of oceanic transform faults: implications for the spatial distribution of seismicity. Geochemistry, Geophysics, and Geosystems 11 (7), Q07001.
Ross, K., Elthon, D., 1997. Extreme incompatible trace-element depletion of diopside in residual mantle from south of the Kane Fracture Zone. In: Karson, J.A., Cannat, M., Miller, D.J., Elthon, D. (Eds.), Proceedings of the Ocean Drilling Program, Scientific Results Vol. 153. College Station, TX, pp. 277–284.
Rubin, K.H., Macdougall, J.D., 1988. ^{226}Ra excesses in mid-ocean-ridge basalts and mantle melting. Nature 335, 158–161.
Rubin, K.H., Sinton, J.M., Maclennan, J., Hellebrand, E., 2009. Magmatic filtering of mantle compositions at mid-ocean-ridge volcanoes. Nature Geoscience 2, 321–328.
Salters, V.J.M., Dick, H.J.B., 2002. Mineralogy of the mid-ocean-ridge basalt source from neodymium isotopic composition of abyssal peridotites. Nature 418, 68–72.
Salters, V.J.M., Stracke, A., 2004. Composition of the depleted mantle. Geochemistry, Geophysics, and Geosystems 5 (5).
Sauter, D., Cannat, M., Rou'ejon, S., Andreani, M., Birot, D., Bronner, A., Brunelli, D., Carlut, J., Delacour, A., Guyader, V., MacLeod, C.J., Manatschal, G., Mendel, V., Ménez, B., Pasini, V., Ruellan, E., Searle, R.C., 2013. Continuous exhumation of mantle-derived rocks at the Southwest Indian Ridge for 11 million years. Nature Geoscience 6 (4), 314–320.
Seyfried, W.E., Foustoukos, D.I., Fu, Q., 2007. Redox evolution and mass transfer during serpentinization: an experimental and theoretical study at 200 °C, 500 bar with implications for ultramafic-hosted hydrothermal systems at mid-ocean ridges. Geochimica et Cosmochimica Acta 71, 3872–3886.
Seyler, M., Bonatti, E., 1997. Regional-scale melt–rock interaction in lherzolitic mantle in the Romanche Fracture Zone (Atlantic Ocean). Earth and Planetary Science Letters 146, 273–287.
Seyler, M., Toplis, M.J., Lorand, J.-P., Luguet, A., Cannat, M., 2001. Clinopyroxene microtextures reveal incompletely extracted melts in abyssal peridotites. Geology 29 (2), 155–158.
Seyler, M., Cannat, M., Mével, C., 2003. Evidence for major-element heterogeneity in the mantle source of abyssal peridotites from the Southwest Indian Ridge (52° to 68°E). Geochemistry, Geophysics, and Geosystems 4 (2), 9101.
Seyler, M., Lorand, J.-P., Toplis, M.J., Godard, G., 2004. Asthenospheric metasomatism beneath the mid-ocean ridge: evidence from depleted abyssal peridotites. Geology 32 (4), 301–304.
Seyler, M., Lorand, J.-P., Dick, H.J.B., Drouin, M., 2007. Pervasive melt percolation reactions in ultra-depleted refractory harzburgites at the Mid-Atlantic Ridge, 15°20′N: ODP Hole 1274A. Contributions to Mineralogy and Petrology 153, 303–319.
Seyler, M., Brunelli, D., Toplis, M.J., Mével, C., 2011. Multiscale chemical heterogeneities beneath the eastern Southwest Indian Ridge (52°E–68°E): trace element compositions of along axis dredged peridotites. Geochemistry, Geophysics, and Geosystems 12 (9), Q0AC15.
Shaw, D.M., 1970. Trace element fractionation during anatexis. Geochimica et Cosmochimica Acta 34, 237–243.
Shibata, T., Thompson, G., 1986. Peridotites from the Mid-Atlantic Ridge at 43°N and their petrogenetic relation to abyssal tholeiites. Contributions to Mineralogy and Petrology 93, 144–159.
Shorttle, O., Maclennan, J., Lambart, S., 2014. Quantifying lithological variability in the mantle. Earth and Planetary Science Letters 395, 24–40.
Sichel, S.E., Esperança, S., Motoki, A., Maia, M., Horan, M.F., Szatmari, P., Alves, E.d.C., Mello, S.L.M., 2008. Geophysical and geochemical evidence for cold upper mantle beneath the equatorial Atlantic Ocean. Revista Brasileira de Geofísica 26 (1), 69–86.
Simon, N.S.C., Neumann, E.-R., Bonadiman, C., Coltorti, M., Delpech, G., Grégoire, M., Widom, E., 2008. Ultra-refractory domains in the oceanic mantle lithosphere sampled as mantle xenoliths at ocean islands. Journal of Petrology 49 (6), 1223–1251.
Sleep, N.H., Barth, G.A., 1997. The nature of oceanic lower crust and shallow mantle emplaced at low spreading rates. Tectonophysics 279, 181–191.
Sleep, N.H., Warren, J.M., 2014. Effect of latent heat of freezing on crustal generation at low spreading rates. Geochemistry, Geophysics, and Geosystems 15, 3161–3174.
Smith, D.K., Escartín, J., Schouten, H., Cann, J.R., 2012. Active long-lived faults emerging along slow-spreading mid-ocean ridges. Oceanography 25 (1), 94–99.
Snow, J.E., 1993. The Isotope Geochemistry of Abyssal Peridotites and Related Rocks Ph.D. Thesis MIT/WHOI Joint Program.
Snow, J.E., Reisberg, L., 1995. Os isotopic systematics of the morb mantle: results form altered abyssal peridotites. Earth and Planetary Science Letters 136, 723–733.
Snow, J.E., Hart, S.R., Dick, H.J.B., 1994. Nd and Sr isotope evidence linking mid-ocean-ridge basalts and abyssal peridotites. Nature 371, 57–60.
Sobolov, A.V., Hofmann, A.W., Kuzmin, D.V., Yaxley, G.M., Arndt, N.T., Chung, S.-L., Danyushevsky, L.V., Elliott, T., Frey, F.A., Garcia, M.O., Gurenko, A.A., Kamenetsky, V.S., Kerr, A.C., Krivolutskaya, N.A., Matvienkov, V.V., Nikogosian, I.K., Rocholl, A., Sigurdsson, I.A., Sushchevskaya, N.M., Teklay, M., 2007. The amount of recycled crust in sources of mantle-derived melts. Science 316 (5823), 412–417.
Spiegelman, M., 1996. Geochemical consequences of melt transport in 2-D: the sensitivity of trace elements to mantle dynamics. Earth and Planetary Science Letters 139, 115–132.
Spiegelman, M., Kelemen, P.B., 2003. Extreme chemical variability as a consequence of channelized melt transport. Geochemistry, Geophysics, and Geosystems 4 (7), 1055.
Standish, J.J., Hart, S.R., Blusztajn, J., Dick, H.J.B., Lee, K.L., 2002. Abyssal peridotite osmium isotopic compositions from Cr-spinel. Geochemistry, Geophysics, and Geosystems 3 (1).
Stephens, C.J., 1997. Heterogeneity of oceanic peridotite from the western canyon wall at MARK: results from Site 920. In: Karson, J.A., Cannat, M., Miller, D.J., Elthon, D. (Eds.), Proceedings of the Ocean Drilling ProgramScientific Results Vol. 153. College Station, TX, pp. 285–303.
Stixrude, L., Lithgow-Bertelloni, C., 2012. Geophysics of chemical heterogeneity in the mantle. Annual Review of Earth and Planetary Sciences 40, 56–595.
Stracke, A., Snow, J.E., Hellebrand, E., von der Handt, A., Bourdon, B., Birbaum, K., Günther, D., 2011. Abyssal peridotite Hf isotopes identify extreme mantle depletion. Earth and Planetary Science Letters 308, 359–368.
Suhr, G., Seck, H.A., Shimizu, N., Günther, D., Jenner, G., 1998. Infiltration of refractory melts into the lowermost oceanic crust: evidence from dunite- and gabbro-hosted clinopyroxenes in the Bay of Islands Ophiolite. Contributions to Mineralogy and Petrology 131, 136–154.
Suhr, G., Hellebrand, E., Snow, J.E., Seck, H.A., 2003. Significance of large, refractory dunite bodies in the upper mantle of the Bay of Islands Ophiolite. Geochemistry, Geophysics, and Geosystems 4 (3), 8605.
Sun, C., Liang, Y., 2012. Distribution of REE between clinopyroxene and basaltic melt along a mantle adiabat: effects of major element composition, water, and temperature. Contributions to Mineralogy and Petrology 163, 807–823.
Sun, C., Liang, Y., 2013a. Distribution of REE and HFSE between low-Ca pyroxene and lunar picritic melts around multiple saturation points. Geochimica et Cosmochimica Acta 119, 340–358.
Sun, C., Liang, Y., 2013b. The importance of crystal chemistry on REE partitioning between mantle minerals (garnet, clinopyroxene, orthopyroxene, and olivine) and basaltic melts. Chemical Geology 358, 23–36.
Sun, C., Liang, Y., 2014. An assessment of subsolidus re-equilibration on REE distribution among mantle minerals olivine, orthopyroxene, clinopyroxene, and garnet in peridotites. Chemical Geology 372, 80–91.
Takahashi, E., Abe, N., Seyler, M., Meurer, W.P., 2007. Hybridization of dunite and gabbroic materials in Hole 1271B from Mid-Atlantic Ridge 15°N: implications for melt flow and reaction in the upper mantle. In: Kelemen, P.B., Kikawa, E., Miller, D.J. (Eds.), Proceedings of the Ocean Drilling Program, Scientific ResultsOcean Drilling Program 209. College Station, TX, pp. 1–23.
Tartarotti, P., Susini, S., Nimis, P., Ottolini, L., 2002. Melt migration in the upper mantle along the Romanche Fracture Zone (Equatorial Atlantic). Lithos 63, 125–149.
van Keken, P.E., Hauri, E.H., Ballentine, C.J., 2002. Mantle mixing: the generation, preservation, and destruction of chemical heterogeneity. Annual Review of Earth and Planetary Sciences 30, 493–525.
Vernières, J., Godard, M., Bodinier, J.-L., 1997. A plate model for the simulation of trace element fractionation during partial melting and magma transport in the Earth's upper mantle. Journal of Geophysical Research 102 (B11), 2471–24784.
Walter, M.J., 1998. Melting of garnet peridotite and the origin of komatiite and depleted lithosphere. Journal of Petrology 39 (1), 29–60.
Walter, M.J., 2014. Melt extraction and compositional variability in mantle lithosphere. In: Carlson, R.W. (Ed.)2nd Edition Treatise on Geochemistry Vol. 3. Elsevier, pp. 393–419 (Ch. 10).

Walter, M.J., Presnall, D.C., 1994. Melting behavior of simplified lherzolite in the system $CaO–MgO–Al_2O_3–SiO_2–Na_2O$ from 7 to 35 kbar. Journal of Petrology 35 (2), 329–359.
Warren, J.M., 2007. Geochemical and Rheological Constraints on the Dynamics of the Oceanic Upper Mantle Ph.D. Thesis Massachusetts Institute of Technology/Woods Hole Oceanographic Institution.
Warren, J.M., Hauri, E.H., 2014. Pyroxenes as tracers of mantle water variations. Journal of Geophysical Research 119 (3), 1851–1881.
Warren, J.M., Shimizu, N., 2010. Cryptic variations in abyssal peridotite composition: evidence for recent melt–rock reaction at the ridge. Journal of Petrology 51, 395–423.
Warren, J.M., Shirey, S.B., 2012. Lead and osmium isotopic constraints on the oceanic mantle from single abyssal peridotite sulfides. Earth and Planetary Science Letters 359–360, 279–293.
Warren, J.M., Shimizu, N., Sakaguchi, C., Dick, H.J.B., Nakamura, E., 2009. An assessment of upper mantle heterogeneity based on abyssal peridotite isotopic compositions. Journal of Geophysical Research 114 (B12203).
Wasylenki, L.E., Baker, M.B., Kent, A.J.R., Stolper, E.M., 2003. Near-solidus melting of the shallow upper mantle: partial melting experiments on depleted peridotite. Journal of Petrology 44 (7), 1163–1191.
White, R.S., McKenzie, D.P., O'Nions, R.K., 1992. Oceanic crustal thickness from seismic measurements and rare earth element inversions. Journal of Geophysical Research 97 (B13), 19683–19715.
White, R.S., Minshull, T.A., Bickle, M.J., Robinson, C.J., 2001. Melt generation at very slow-spreading oceanic ridges: constraints from geochemical and geophysical data. Journal of Petrology 42 (6), 1171–1196.
Workman, R.K., Hart, S.R., 2005. Major and trace element composition of the depleted MORB mantle (DMM). Earth and Planetary Science Letters 231, 53–72.
Yao, L., Sun, C., Liang, Y., 2012. A parameterized model for REE distribution between low-Ca pyroxene and basaltic melts with applications to REE partitioning in low-Ca pyroxene along a mantle adiabat and during pyroxenite-derived melt and peridotite interaction. Contributions to Mineralogy and Petrology 164, 261–280.
Zhou, H., Dick, H.J.B., 2013. Thin crust as evidence for depleted mantle supporting the Marion Rise. Nature 494, 195–200.
Zindler, A., Hart, S., 1986. Chemical geodynamics. Annual Review of Earth and Planetary Sciences 14, 493–571.
Zindler, A., Staudigel, H., Batiza, R., 1984. Isotope and trace element geochemistry of young Pacific seamounts: implications for the scale of upper mantle heterogeneity. Earth and Planetary Science Letters 70, 175–195.
Zou, H., 1998. Trace element fractionation during modal and nonmodal dynamic melting and open-system melting: a mathematical treatment. Geochimica et Cosmochimica Acta 62, 1937–1945.